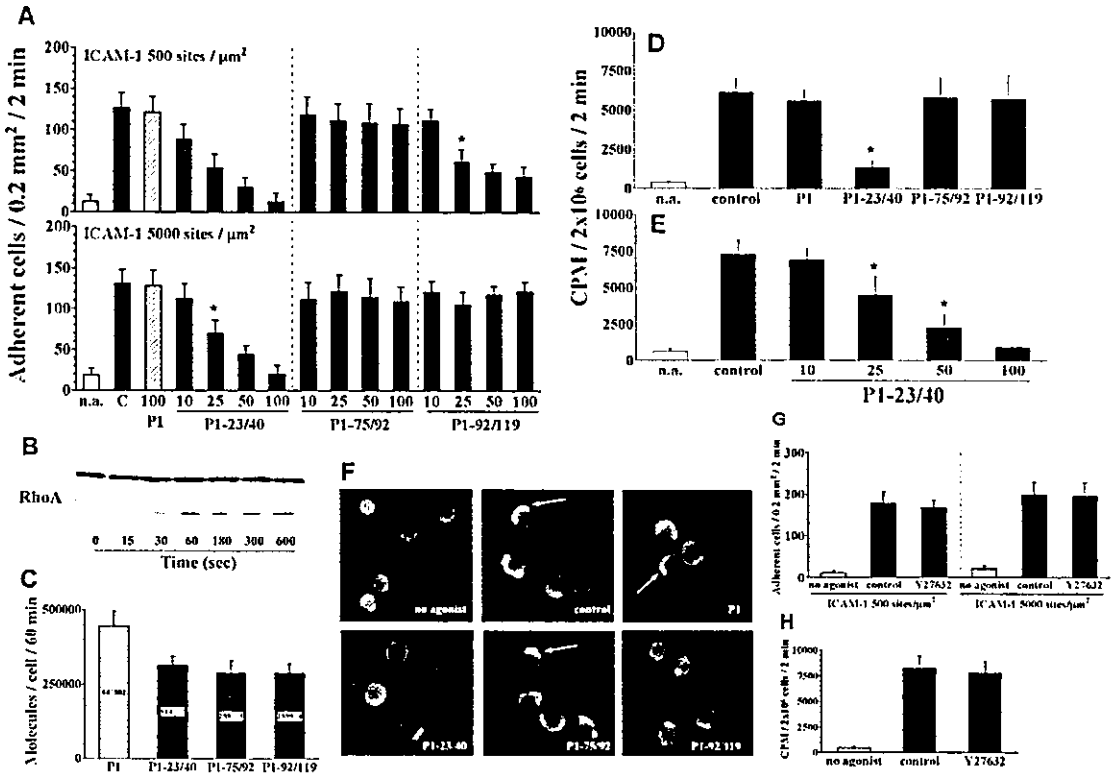

Figure 2. RhoA Control LFA-1 High-Affinity State and Lateral Mobility Triggering by CCL21

(A) ICAM-1 was immobilized at the indicated site densities. Lymphocytes were treated at 37°C for 60 min with buffer (n.a. and C) or with the indicated μM doses of P1 or different P1-RhoA peptides and then stimulated for 2 min with buffer (n.a., no agonist) or with 1 μM CCL21. Values are mean counts of adherent cells in six to nine experiments. Error bars are SDs. *$p < 0.01$.

(B) Lymphocytes were stimulated at 37°C under stirring with 1 μM CCL21 for the indicated time; time 0 corresponds to no agonist. A protein immunoblot of anti-RhoA in lysates (top) and precipitates (bottom) is shown. One representative experiment of three.

(C) Lymphocytes were treated at 37°C for 60 min with 100 μM of ^{125}I P1 or P1-RhoA peptides. Values are the mean numbers of internalized molecules per cell in three experiments. Error bars are SDs.

(D and E) (D) RhoA controls the induction of LFA-1 high-affinity state by CCL21. Lymphocytes were treated at 37°C for 60 min with buffer (n.a. and control), with 100 μM of P1 or different P1-RhoA peptides, or (E) with the indicated concentrations of P1-23/40 RhoA region, and then stimulated for 2 min with buffer (no agonist) or with 1 μM CCL21. The mean CPM from ^{125}I-ICAM-1 in three experiments is shown. Error bars are SDs. *$p < 0.01$.

(F) RhoA controls the induction of LFA-1 rapid lateral mobility on the plasma membrane induced by CCL21. Lymphocytes were treated as described for (D), and then stimulated at 37°C for 2 min with 1 μM CCL21. Confocal images of LFA-1 surface distribution are shown. Arrows indicate LFA-1 clusters.

(G) ICAM-1 was immobilized at the indicated site densities. Lymphocytes were treated at 37°C 30 min with buffer (n.a. and control) or with 50 μM Y27632 and then stimulated for 2 min with buffer (no agonist) or with 1 μM CCL21. Values are the mean counts of adherent cells in three experiments. Error bars are SDs.

(H) Lymphocytes were treated with 50 μM Y27632. LFA-1 affinity triggering was evaluated as described for (D). Values are from three experiments. Error bars are SDs.

Distinct RhoA Effector Regions Control Chemokine-Induced LFA-1-Dependent Rapid Lymphocyte Adhesion to ICAM-1

To evaluate the role of RhoA in the complex modality of LFA-1 activation by chemokines, we first investigated the involvement of RhoA in CCL21-induced rapid LFA-1-dependent lymphocyte adhesion to ICAM-1 immobilized at either low or high site densities. When lymphocytes were stimulated to adhere to low density of ICAM-1 (~500 sites/μm²), both 23–40 and 92–119 P1-RhoA peptides prevented in a dose-dependent manner rapid adhesion induced by CCL21 (Figure 2A). In contrast, the 75–92 P1-RhoA peptide or the P1 peptide was unable to block rapid adhesion triggering. However, on high density of ICAM-1 (~5000 sites/μm²), only the 23–40 P1-RhoA peptide blocked adhesion triggering in a dose-dependent manner, whereas P1, 75–92, and 92-119 P1-RhoA peptides were ineffective (Figure 2A). None of the used peptides interfered with intracellular calcium increase induced by CCL21, thus ruling out potential nonspecific effects (data not shown). RhoA involvement in CCL21-induced LFA-1-dependent lymphocyte adhesion was further corroborated by biochemical analysis showing that CCL21 activated RhoA within seconds, thus displaying kinetics consistent with rapid LFA-1 triggering (Figure 2B). To exclude that the difference be-

Table 1. Quantitative Analysis of the Effect of RhoA, ROCK, and ζ PKC Inhibition on LFA-1 Plasma Membrane Distribution by CCL21

		LFA-1 Distribution on Plasma Membrane	
		Disperse (%)	Clusters (%)
	No agonist	88 ± 14	12 ± 8
CCL21	Control	21 ± 10	79 ± 11
	Penetratin-1 (P1)	30 ± 17	70 ± 13
	P1-23/40	60 ± 14	40 ± 16
	P1-75/92	14 ± 10	86 ± 11
	P1-92/119	79 ± 13	21 ± 8
	Y27632	23 ± 12	77 ± 14
	Myr-α PKC	22 ± 5	78 ± 12
	Myr-δ PKC	17 ± 8	83 ± 16
	Myr-ε PKC	25 ± 10	75 ± 11
	Myr-ζ scramble	19 ± 9	81 ± 19
	Myr-ζ PKC	81 ± 18	19 ± 7

Lymphocytes were treated with buffer (Control), 50 μM P1 or different P1-RhoA peptides, 50 μM of Y27632 or with 100 μM of PKC myristoylated pseudosubstrate peptides, and then stimulated for 2 min with buffer (no agonist) or with 1 μM CCL21. At least 100 cells for each data point were analyzed. Values are mean ± SD percentage of analyzed cells in three experiments.

tween P1-RhoA peptides in lymphocytes could be due to unequal accumulation of the peptides into the cell, we calculated the number of molecules of different peptides loaded per single cell. Although the P1 peptide loaded more efficiently, all three different P1-RhoA peptides showed a similar capability to accumulate inside lymphocytes (Figure 2C).

Together, these data show that RhoA controls LFA-1 activation by CCL21 through the signaling activity of two distinct effector regions.

Distinct RhoA Effector Regions Control the Different Modalities of LFA-1 Activation by Chemokines

Chemokine-triggered lymphocyte arrest in condition of variable density of ICAM-1 relies on distinct intracellular signaling pathways specifically controlling the two modalities of LFA-1 activation (Constantin et al., 2000). Thus, the previous data strongly suggest that RhoA activates both modalities of LFA-1-activation through the distinct signaling activity of 23–40 and 92–119 effector regions. To test this hypothesis, we evaluated the capability of different P1-RhoA peptides to interfere with LFA-1 high-affinity state and rapid lateral mobility triggering by chemokines. Pretreatment with the P1 control or the 75–92 and 92–119 P1-RhoA peptides did not prevent LFA-1 high-affinity state triggering (Figure 2D). In contrast, pretreatment of lymphocytes with the 23–40 P1-RhoA peptide prevented heterodimer high-affinity state induction by CCL21 (Figure 2D). Inhibition of LFA-1 high-affinity state triggering by the 23–40 P1-RhoA peptide was dose dependent and almost complete, with a maximum blockade of about 90% (Figure 2E).

We next determined the involvement of RhoA in the induction of rapid LFA-1 lateral mobility by CCL21. Pretreatment with the P1 control peptide or with the 75–92 P1-RhoA peptide did not prevent LFA-1 rapid lateral mobility induced by CCL21. In contrast, pretreatment with both 23–40 and 92–119 P1-RhoA peptides prevented rapid generation of LFA-1 clusters (Figure 2F and Table 1).

Taken together, these data show that RhoA controls both modalities of chemokine-induced rapid LFA-1 activation by means of distinct effector regions. Interestingly, the 75–92 effector region, involved in ROCK activation, does not appear to have a role in chemokine-induced integrin activation. Notably, 23–40 and 92–119 RhoA regions have been also implicated in ROCK activation (Fujisawa et al., 1998). Therefore, we wished to determine whether ROCK could be an effector in RhoA-dependent LFA-1 rapid activation by chemokines. Pretreatment of lymphocytes with Y27632, a specific ROCK inhibitor (Uehata et al., 1997), did not inhibit CCL21-induced lymphocyte adhesion to ICAM-1 immobilized either at low or high site density (Figure 2G). Furthermore, neither LFA-1 affinity triggering (Figure 2H) nor induction of lateral mobility (Table 1) were blocked by Y27632. These data rule out ROCK as a possible downstream signaling effector linking RhoA to rapid LFA-1 activation by chemokines.

The Atypical ζ PKC Is Involved in Chemokine-Induced LFA-1-Dependent Rapid Lymphocyte Adhesion to ICAM-1

Previous data proposed ζ PKC as potential RhoA effector implicated in Mac1 activation by chemoattractants in polymorphonuclear cells (PMNs) (Laudanna et al., 1998). To evaluate the role of ζ PKC in rapid LFA-1 triggering by chemokines in lymphocytes, we used myristoylated peptides with sequence identical to the pseudosubstrate inhibitory region of ζ PKC (Laudanna et al., 1998). As shown in Figure 3A, blockade of ζ PKC activity inhibited in a dose-dependent manner adhesion triggering to ICAM-1 induced by CCL21. Notably, the inhibitory effect of the ζ PKC peptide was evident only on low density of ICAM-1. Moreover, a control peptide, with a scrambled sequence (Figure 3A), as well as peptides with sequence identical to the pseudosubstrate region of α, δ, and ε PKCs (Figure 3B) were completely unable to prevent adhesion triggering either on low or high density of ICAM-1. To further corroborate the involvement of ζ PKC in signaling pathways generated by chemokines and leading to LFA-1 activation, we analyzed the activation state of ζ PKC upon CCL21 stimulation. As shown in Figure 3C, CCL21 induced a consistent and rapid increase of ζ PKC kinase activity. We also evaluated the intracellular distribution of ζ PKC. As shown in Figure 3D, in resting lymphocytes ζ PKC was mainly associated with the particulate fraction, whereas it was almost absent in the cytosol and plasma membrane. Upon triggering with CCL21, ζ PKC rapidly translocated to the plasma membrane fraction. These data show that the atypical ζ PKC is the only PKC isoform expressed in lymphocytes selectively involved in rapid LFA-1 triggering by chemokines. Importantly, ζ PKC seems relevant only to adhesion to low density of ICAM-1.

The Atypical ζ PKC Controls LFA-1 Lateral Mobility but Not High-Affinity State Induction by Chemokines

The previous data suggest a role for ζ PKC in LFA-1 lateral mobility but not high-affinity state induction by CCL21. To validate this hypothesis we determined the

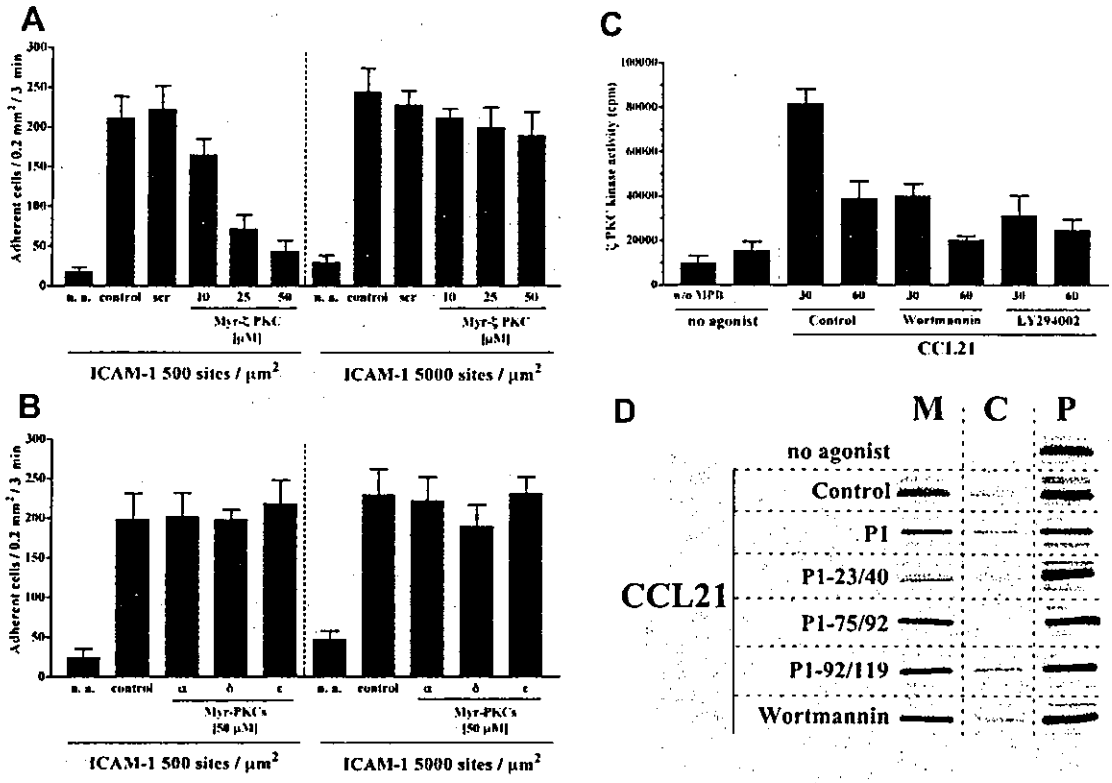

Figure 3. ζ PKC Is Involved in LFA-1 Activation by CCL21

(A) ICAM-1 was immobilized at the indicated site densities. Lymphocytes were treated at 37°C for 60 min with buffer (n.a. and control) or with 50 μM of a scramble peptide (scr) or with the indicated doses of ζ PKC myristoylated pseudosubstrate peptides and then stimulated for 3 min with buffer (n.a., no agonist) or with 1 μM CCL21. Values are the mean counts of adherent cells in five experiments. Error bars are SDs.

(B) ICAM-1 was immobilized at the indicated site densities. Lymphocytes were treated at 37°C for 60 min with buffer (n.a. and control) or with the indicated dose of various PKC myristoylated pseudosubstrate peptides and then stimulated for 3 min with buffer (no agonist) or with 1 μM CCL21. Values are the mean counts of adherent cells in four experiments. Error bars are SDs.

(C) Lymphocytes were treated at 37°C for 30 min with buffer (no agonist and control) or with 150 nM Wortmannin or 30 μM LY294002 and then stimulated at 37°C under stirring for 30 or 60 s with buffer (no agonist) or with 1 μM CCL21. No agonist w/o MBP is radioactive in the absence of exogenous substrate and is a measurement of ζ PKC autophosphorylating activity in nonstimulated lymphocytes. Values are the mean counts of two experiments performed in duplicate. Error bars are SDs.

(D) Lymphocytes were treated at 37°C for 30 min with buffer (no agonist and control), with 100 μM of P1 or P1-RhoA peptides, or with 150 nM Wortmannin and then stimulated at 37°C under stirring for 30 s with buffer (no agonist) or with 1 μM CCL21. Shown are protein immunoblots of cytosolic (C), light membrane (M), and particulate (P) fractions separated on sucrose gradient and probed with anti-ζ PKC Ab.

role of ζ PKC in LFA-1 high-affinity state and lateral mobility induction by CCL21. As shown in Figure 4A, pretreatment of lymphocytes with ζ PKC inhibitory peptides or with a scrambled peptide did not prevent the rapid and transient induction of LFA-1 high-affinity state induced by CCL21. α, δ, and ε PKC inhibitory peptides were also unable to block LFA-1 high-affinity state induction (data not shown). However, confocal microscopy analysis showed that pretreatment of lymphocytes with the ζ PKC inhibitory peptide, but not with a scrambled peptide, prevents the accumulation of large LFA-1 clusters rapidly induced by CCL21 (Figure 4B and Table 1). α, δ, and ε PKC blocking peptides were completely unable to inhibit LFA-1 cluster formation induced by CCL21 (Table 1).

Together, these data show that classical, novel, and atypical PKCs isoforms expressed in lymphocytes are not involved in LFA-1 high-affinity state triggering by CCL21. In contrast, the atypical isoform ζ PKC is necessary for LFA-1 lateral mobility on the plasma membrane induced by CCL21.

The Role of PI(3)K and RhoA in ζ PKC Activation by Chemokines

PI(3)K has been previously implicated in LFA-1 lateral mobility (Constantin et al., 2000) as well as in ζ PKC activation (Le Good et al., 1998). As shown in Figure 3C, pretreatment of lymphocytes with Wortmannin or with LY234002, two PI(3)K specific inhibitors, partially prevented the increase of ζ PKC kinase activity induced by CCL21 (about 51% for Wortmannin and 62% for LY294002). In contrast, pretreatment with PI(3)K inhibitor did not affect ζ PKC translocation to the plasma membrane (Figure 3D). Thus, PI(3)K partially mediates CCL21-induced increase of kinase activity but not trans-

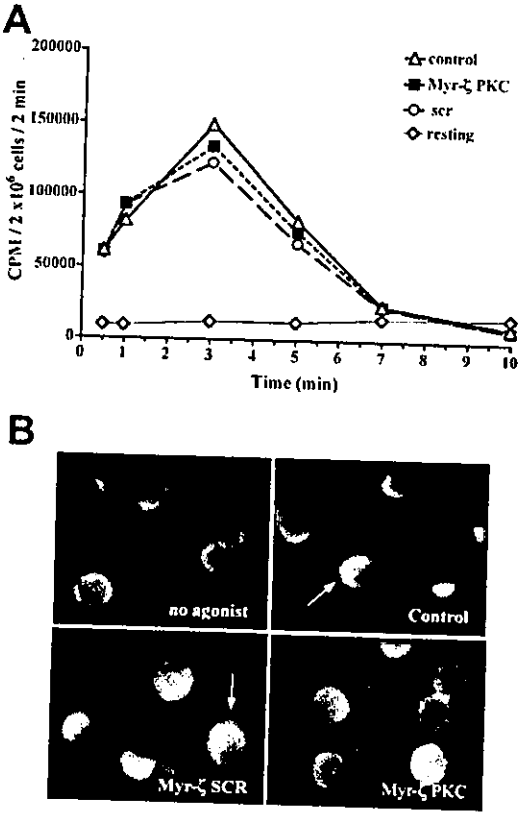

Figure 4. ζ PKC Control LFA-1 Lateral Mobility but Not High-Affinity State Triggering by CCL21

(A) Lymphocytes were treated at 37°C for 60 min with buffer (no agonist and control), or with 50 μM scramble peptide (scr) or ζ PKC myristoylated pseudosubstrate peptide and then stimulated for 2 min with buffer (no agonist) or with 1 μM CCL21. The mean CPM from ^{125}I-ICAM-1 is shown. Values are counts from a representative experiment of three.

(B) Lymphocytes were treated as in (A) and then stimulated at 37°C for 2 min with 1 μM CCL21. Confocal images of LFA-1 surface distribution are shown. Arrows indicate LFA-1 clusters.

location of ζ PKC to the plasma membrane in lymphocytes.

Chemoattractant-induced ζ PKC translocation to the plasma membrane relies on RhoA activity in PMNs (Laudanna et al., 1998). Having identified RhoA downstream effector regions critical to rapid LFA-1 triggering, we had the possibility to investigate the involvement of distinct RhoA effector regions in ζ PKC translocation induced by chemokines in lymphocytes. As shown in Figure 3D, pretreatment of lymphocytes with P1 peptide or with 75–92 or 92–119 P1-RhoA peptides did not prevent ζ PKC translocation to the plasma membrane. However, pretreatment with the 23–40 P1-RhoA peptide blocked ζ PKC translocation to the plasma membrane; the densitometric analysis showed a blockade of about 82%.

These data show that induction of ζ PKC kinase activity by CCL21 in lymphocytes partially depends on PI(3)K, whereas ζ PKC tranlocation to the plasma membrane is mainly controlled by a restricted subset of RhoA-dependent signaling activated by the 23–40 downstream effector region.

RhoA-Dependent LFA-1 High-Affinity State Is the Modality of Integrin Activation Controlling Lymphocyte Homing In Vivo

The data presented above establish diversified roles for RhoA and ζ PKC in controlling distinct modalities of LFA-1 activation. Previous data suggested a role for LFA-1 triggered to high-affinity state in lymphocyte homing to secondary lymphoid organs. However, a formal demonstration has never been provided. The definition of the role of 23–40 RhoA region in LFA-1 high-affinity state triggering by chemokines prompted us to pursue a formal demonstration of the role of LFA-1 triggering to high-affinity state in the recruitment of circulating lymphocytes in vivo.

Pretreatment of lymphocytes with the P1 control peptide or with the 75–92 or 92–119 P1-RhoA peptides did not affect rolling and arrest of circulating lymphocytes on high endothelial venules in the secondary lymphoid organ Peyer's patch (PP-HEV) (Figure 5). Pretreatment with the 23–40 P1-RhoA peptide did not influence lymphocyte tethering and allowed normal interaction with vessels (data not shown). However, this peptide consistently inhibited the stable arrest of lymphocytes on PP-HEV, with about 75% of inhibition ($p < 0.01$); the percentage of cells displaying only rolling increased, as expected. Notably, the site density of ICAM-1 presented to the interacting lymphocytes on PP-HEV was previously shown to be extremely high (about 14,000 site/μm^2) (Constantin et al., 2000), a condition in which LFA-1 accelerated lateral mobility is not required to rapid arrest. Indeed, the 92–119 P1-RhoA peptide, which only affected LFA-1 rapid lateral mobility induced by CCL21, had no effect on lymphocyte arrest in PP-HEV. As the 23–40 RhoA effector region controls the induction of LFA-1 conformational change by CCL21 (see Figure 2), these data demonstrate that RhoA-controlled heterodimer high-affinity state is the modality of LFA-1 activation critically required for rapid arrest of circulating lymphocytes in PP-HEV.

We also wished to test the role of ROCK kinase and ζ PKC in rapid lymphocytes recruitment to HEV. Lymphocytes pretreated with Y27632 rolled and adhered normally in HEV. Moreover, pretreatment of lymphocytes with the ζ PKC inhibitory peptide did not affect the capability of lymphocytes to roll and arrest on HEV (Figure 5). These data are consistent with the inability of these inhibitors to prevent LFA-1 affinity triggering by CCL21 and exclude a participation of ROCK and ζ PKC in signaling events leading to lymphocyte rapid arrest in PP-HEV.

Discussion

Chemokines are the most powerful physiological activators of lymphocyte integrins (Laudanna et al., 2002). We have previously shown that chemokines play a dual role in LFA-1-mediated rapid lymphocyte adhesion by inducing LFA-1 high-affinity state and lateral mobility (Constantin et al., 2000). Here we have identified intracellular signaling events differently controlling this complex

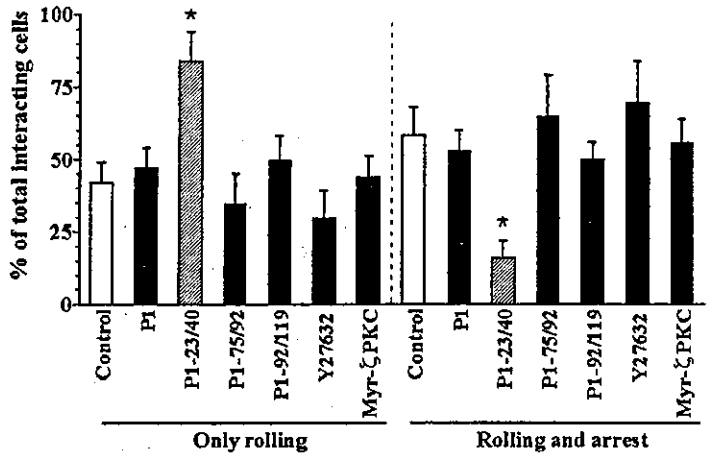

Figure 5. LFA-1 High-Affinity State Mediates Lymphocyte Homing to HEV in Peyer's Patches

Intravital microscopy was performed in Peyer's patch high endothelial venules. Lymphocytes were treated with buffer (control) or with 50 μM P1 and P1-RhoA peptides, with 50 μM Y27632, or with 100 μM of ζ PKC myristoylated pseudosubstrate peptide. Values are the mean percentage of total interacting cells in three experiments. Error bars are SDs. *$p < 0.01$.

phenomenon. We presented data regarding the CCR7 ligand CCL21 which directs T lymphocyte arrest in secondary lymphoid organs (Warnock et al., 2000). However, identical results have been obtained with CCL19 and with the CXCR4 ligand CXCL12 (data not shown), thus supporting the general significance of our findings.

We show that: (1) RhoA controls LFA-1 high-affinity state triggering by chemokines; (2) RhoA also controls LFA-1 lateral mobility induced by chemokines; (3) the signaling activity of two distinct RhoA effector regions controls LFA-1 activation by chemokines; (4) the atypical ζ PKC is critical to LFA-1 lateral mobility but not to high-affinity state triggering; (5) chemokine-induced ζ PKC kinase activity and translocation to the plasma membrane depend, respectively, on PI(3)K and on the signaling activity of the 23–40 RhoA effector region; and (6) rapid arrest of circulating lymphocytes on HEV in secondary lymphoid organs critically depends on the induction of LFA-1 high-affinity state.

RhoA and the Modality of LFA-1 Activation by Chemokines

We showed that plasma membrane translocating RhoA-derived effector regions are useful tools for studying RhoA-dependent signaling events in a region-selective manner. The inhibitory, more than agonistic, activity of the regions is likely due to interference with the plasma membrane docking function of small GTPases, a step required to full activation of downstream effectors (Stokoe et al., 1994). By using these tools, we analyzed the role of RhoA in LFA-1-dependent rapid lymphocyte adhesion. Our data show that RhoA controls LFA-1 conformational change and lateral mobility by chemokines through the distinct, yet complementary, activity of two effector regions, encompassing amino acids 23–40 and 92–119. The 92–119 region is exclusively involved in LFA-1 lateral mobility induction. In contrast, the 23–40 RhoA region participates in heterodimer lateral mobility regulation and is also critical to the induction of LFA-1 high-affinity state. This latter finding is of particular importance. Indeed, the intracellular signaling events controlling LFA-1 high-affinity state triggering by chemokines and the physiological meaning of this event have never been clarified. The blocking activity of the P1-23-40 peptide on LFA-1 affinity triggering by CCL21 highlighted the critical regulatory role of RhoA in LFA-1 high-affinity triggering. Importantly, blockade of 23–40 RhoA effector region prevented LFA-1-dependent arrest of naive lymphocytes on PP-HEV. Although 23–40 RhoA region also controls LFA-1 lateral mobility, blockade of the 92–119 region, which is only involved in heterodimer lateral mobility, did not interfere with arrest of naive lymphocytes on PP-HEV. This shows that lymphocytes rely on activation of LFA-1 high-affinity state to home to secondary lymphoid organs. This provides the definitive demonstration of the physiological role of the inside-out signal-dependent induction of LFA-1 high-affinity state in vivo.

Biochemical analysis showed a rapid and prolonged RhoA activation by CCL21, with RhoA remaining in an active state for at least 10 min. Notably, the induction of LFA-1 high-affinity state by chemokines displays transient kinetics, with integrin affinity completely downmodulated within a few minutes (Constantin et al., 2000). This suggests that downmodulation of LFA-1 high-affinity state, which temporally correlates with downmodulation of lymphocyte rapid adhesion to ICAM-1, does not simply rely on RhoA inactivation. Thus, it is possible that chemokines generate signaling pathways able to actively counterbalance RhoA-dependent pathways leading to LFA-1 conformational changes. Notably, the activation of H-ras and the dependent MAP-kinase prevents the induction of LFA-1 high-affinity state by the chemokine CXCL12 (Weber et al., 2001b). Thus, it is possible that a temporally and spatially regulated balance between the signaling activities of H-ras and RhoA could regulate the dynamics of LFA-1 high-affinity state activation and dependent rapid adhesion.

ζ PKC and the Modality of LFA-1 Activation by Chemokines

To deepen the investigation, we determined the involvement of the atypical ζ PKC in LFA-1 activation by chemokines. ζ PKC was found to be critical for LFA-1 lateral mobility but not high-affinity state triggering by CCL21. Notably, we have previously shown that LFA-1 lateral

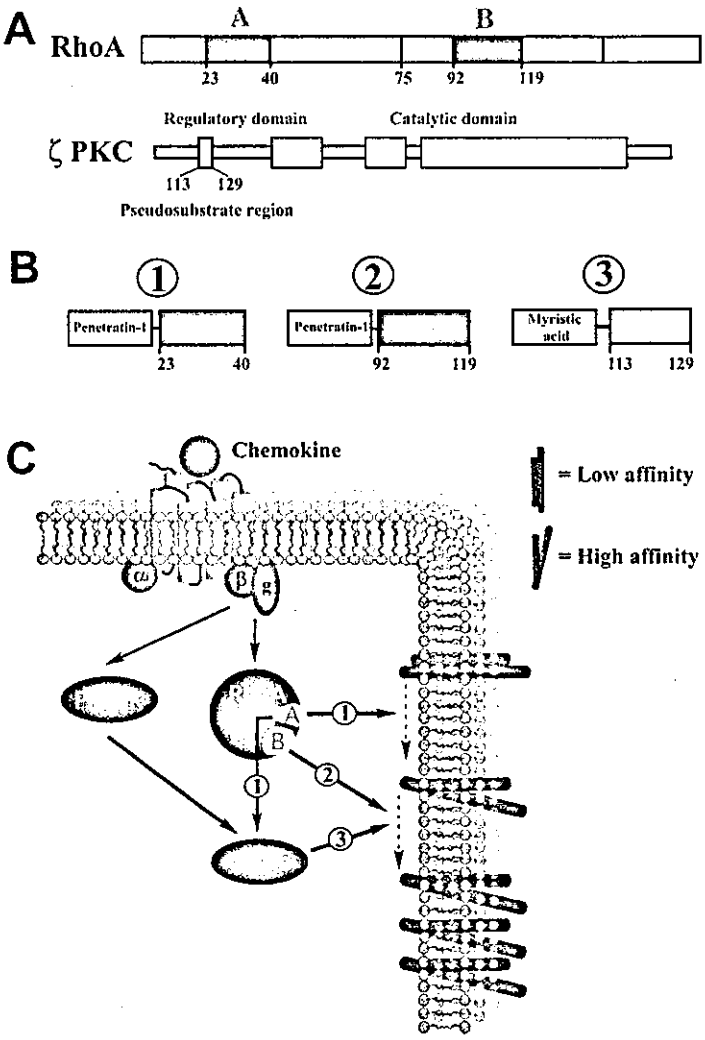

Figure 6. The Distinct Roles of RhoA and ζ PKC in the Different Modalities of Rapid LFA-1 Activation by Chemokines

(A) Site organization of RhoA and ζ PKC showing the effector regions of RhoA (aa 23–40 [A], 75–92 and 92–119 [B]), and the inhibitory pseudosubstrate region of ζ PKC (aa 113–129).

(B) The plasma membrane translocating peptides displaying inhibitory capability on LFA-1 activation. The 23–40 (1) and 92–119 (2) RhoA effector regions were fused to Penetratin-1. A myristic acid was added N-terminal of the pseudosubstrate region of ζ PKC (3).

(C) Induction of LFA-1 high-affinity state by chemokines is controlled by the signaling activity of 23–40 downstream effector region of RhoA (marked with A). Induction of LFA-1 lateral mobility is controlled by ζ PKC and by further signals generated by the 92–119 downstream effector region of RhoA (marked with B). The capability of ζ PKC to control LFA-1 lateral mobility depends on translocation to the plasma membrane, which is controlled by the RhoA 23–40 downstream effector region, as well as by ζ PKC kinase activity. ζ PKC appears to be an effector of both PI(3)K and RhoA mediating LFA-1 lateral mobility induced by chemokines. (1) Inhibition by the P1-RhoA 23–40 peptide. (2) Inhibition by the P1-RhoA 92–119 peptide. (3) Inhibition by the myristoylated peptide with sequence identical to ζ PKC pseudosubstrate region.

mobility is not involved in lymphocyte in vivo homing (Constantin et al., 2000). Therefore, it is not surprising that ζ PKC has no role in in vivo lymphocyte homing to PP. However, as we previously suggested for PI(3)K, ζ PKC could have a role in lymphocyte recruitment to vessels expressing low density of integrin ligand, a situation in which heterodimer lateral mobility is required for lymphocyte arrest under flow.

Of interest, we also found that the slow LFA-1 clustering induced by PMA is sensitive to ζ PKC blockade (data not shown). Accordingly, we previously showed that PMA, although not an allosteric activator of ζ PKC (atypical PKCs have incomplete C1 region), may trigger ζ PKC translocation to the plasma membrane through RhoA activation (Laudanna et al., 1998). Notably, ζ PKC has a constitutive kinase activity, and this implies that ζ PKC translocation to the plasma membrane may be sufficient to generate ζ PKC-dependent signaling events even in the absence of augmented kinase activity.

The ability of the 23–40 P1-RhoA peptide to block ζ PKC translocation suggests that ζ PKC may mediate, at least partially, the RhoA capability to control LFA-1 clustering. Moreover, this data suggests a direct interaction between RhoA and ζ PKC, thus establishing ζ PKC as a potential direct downstream effector of RhoA. This possibility is also supported by a previous report (Slater et al., 2001). However, it is also possible that ζ PKC translocation is mediated by other RhoA-dependent signaling events. For instance, PLD is activated by direct binding with the RhoA switch I region (encompassed by the 23–40 sequence) (Dae Bae et al., 1998), and PLD-derived phosphatidic acid (PA) is a powerful ζ PKC activator (Limatola et al., 1997). Thus, it is possible that the inhibitory effect of the 23–40 P1-RhoA peptide on ζ PKC translocation is due to PLD inhibition. Further studies are required to test these possibilities.

The Complexity of the Chemokine-Induced Proadhesive Signaling Network

The data presented here, together with previous reports, further highlight the bewildering complexity of the signaling network generated by chemokines and leading

to integrin activation. Chemokine-triggered LFA-1 lateral mobility is controlled at least by PI(3)K, Cytohesin-1, Rap1, ζ PKC, and RhoA. This brings into question the network relationship that these signaling molecules have. Recruitment of Cytohesin-1 to the plasma membrane requires PI(3)K activity (Nagel et al., 1998). Moreover, PI(3)K-derived PIP3 increases ζ PKC activity, and the PIP3-dependent kinase PDK-1 is a direct activator of ζ PKC (Le Good et al., 1998). Thus, PI(3)K appears to control both Cytohesin-1 and ζ PKC signaling activity leading to LFA-1 lateral mobility and clustering. However, regulation of ζ PKC does not seem to be dependent on only PI(3)K. Indeed, inhibition of PI(3)K does not totally prevent the increase of ζ PKC kinase activity induced by CCL21 and does not block translocation of ζ PKC to the plasma membrane. In contrast, ζ PKC translocation to the plasma membrane is critically dependent on signaling activity of RhoA 23–40 effector region. Altogether, these data show that ζ PKC translocation to the plasma membrane and increase of kinase activity are independently controlled by distinct signaling pathways.

Are both of these regulatory mechanisms of ζ PKC equally relevant to the activation of LFA-1 lateral mobility on the plasma membrane? Inhibition of PI(3)K blocks chemokine-induced, but not PMA-triggered, LFA-1 clustering (Constantin et al., 2000). In contrast, blockade of ζ PKC by inhibitory peptides prevents LFA-1 clustering induced by chemokines as well as by PMA. Thus, ζ PKC translocation to the plasma membrane (which is RhoA dependent in PMA as well as chemokine-triggered signaling) is a very critical biochemical event in LFA-1 clustering. What is the role of the increased ζ PKC kinase activity triggered by chemokines? It is important to emphasize that chemokines trigger within seconds formation of big LFA-1 clusters in lymphocytes, whereas PMA induces smaller LFA-1 clusters over several minutes (Constantin et al., 2000). In this context, we previously hypothesized that PI(3)K, which is not activated by PMA, could be responsible for acceleration in LFA-1 lateral mobility induced by chemokines (Constantin et al., 2000). The critical role of ζ PKC in LFA-1 clustering and the capability of PI(3)K to partially mediate the increase of ζ PKC activity induced by CCL21 allow a further refinement of our previous hypothesis. Thus, it is possible that RhoA-mediated ζ PKC translocation triggered by PMA in the absence of any PI(3)K activation (and thus without increase of ζ PKC activity) may be sufficient to induce a slow LFA-1 lateral mobility on the plasma membrane. In contrast, the very rapid LFA-1 mobility induced by chemokines may require both RhoA-mediated ζ PKC translocation and a concurrent PI(3)K-dependent increase of ζ PKC kinase activity. We then hypothesize that a consistent increase of the kinase activity of ζ PKC is critical to the acceleration of LFA-1 lateral mobility on the plasma membrane observed upon chemokine stimulation and required for rapid lymphocyte arrest in conditions of low density of integrin ligand. It will be of great interest to test this hypothesis under experimental conditions allowing a more accurate evaluation of the kinetics of LFA-1 lateral mobility at the single molecule level.

Importantly, RhoA controls LFA-1 lateral mobility also through the engagement of the 92–119 effector region, which is not involved in ζ PKC translocation, suggesting that further RhoA-activated signals are necessary to allow LFA-1 mobility on the plasma membrane. Furthermore, recent reports show that additional signals may derive from the activity of the small GTPase Rap1 (Shimonaka et al., 2003). Thus, chemokines trigger at least three independent, yet necessary, signaling pathways controlled by PI(3)K, Rap1, and RhoA, whose integration generates a signaling network controlling LFA-1 accelerated lateral mobility on the plasma membrane.

In conclusion, we show that RhoA and ζ PKC are critical components of the signaling network controlling the complex dynamic of activation of the β2 integrin LFA-1. The small GTP binding protein RhoA is a central point of diversification of signaling pathways controlling both the modalities of LFA-1 activation induced by chemokines. In contrast, ζ PKC is a point of convergence of signaling events controlling only LFA-1 lateral mobility (Figure 6). Importantly, we formally demonstrate the critical role of LFA-1 affinity triggering in lymphocyte in vivo homing to PP. Our data suggest that a generic, region-nonspecific, pharmacological inhibition of RhoA would not be the most rational approach for a potential pharmacological intervention in RhoA-dependent phenomena. Indeed, a global inhibition of RhoA-dependent signaling activity may prevent LFA-1 high-affinity state triggering and, thus, block lymphocyte recirculation in secondary lymphoid organs, an event that is likely to result in undesired side effects. In contrast, selective blockade of the 92–119 RhoA region could exclusively inhibit LFA-1 lateral mobility without affecting lymphocyte homing to secondary lymphoid organs. This modality of LFA-1 activation was previously postulated to be relevant in the case of variable density of ICAM-1 expressed by the microvasculature, such as during inflammation (Constantin et al., 2000). Thus, the identification of discrete RhoA effector regions controlling distinct modalities of LFA-1 activation may help to devise a more effective pharmacological approach to control leukocyte recruitment during inflammation.

Experimental Procedures

Materials

PKC myristoylated pseudosubstrate peptides (synthesized at Stanford University PAN-facility) were dissolved before use at 1 mM concentration in PBS (pH 7.2). PMA, ketamine, and xylosine were from Sigma; FCS was from Irvine; murine CCL21 and CXCL12 were form Peprotech (London, United Kingdom); CMFDA, CMTMR, and Alexa 488 labeling kit were from Molecular Probes; Texas red-conjugated goat anti-rat antibody was from Jackson ImmunoResearch; murine ICAM-1 was purified from spleens (Constantin et al., 2000).

Generation of Penetratin-1-RhoA Peptides

The Penetratin-1 (P1) fusion protein expression vector pTm3Hb was kindly donated by A. Prochiantz (CNRS, France). Oligonucleotides encompassing human RhoA bases 67–120 (aa 23–40), 223–276 (aa 75–92), and 274–357 (aa 92–119) were inserted between the BamHI and KpnI cloning sites. Recombinant proteins expressed in *E. coli* BL21(DE3)pLysS Gold were purified on heparin columns, dialyzed against PBS, and stored at −80°C. Alternatively, P1, P1-23-40, and P1-75-92 peptides were synthesized by Sigma-Genosys. A glycine was inserted between P1 and RhoA regions to allow flexibility of the peptides. Peptides displayed the following properties: P1, aa 16, mw 2246.78; P1-RhoA 23-40, aa 34, mw 4430.29; P1-RhoA 75-92, aa 34, mw 4254.06; P1-RhoA 92–119, aa 44, mw 5529.83. Lyophilized peptides were dissolved before the experiments.

Specificity of RhoA Peptides and Measurement of RhoA Activation

The specificity of P1-RhoA peptides was evaluated by affinity-precipitation assay using the rho binding region (RBD) from Citron, Rhotekin, and ROCK, as described (Ren et al., 1999; Kimura et al., 2000). Recombinant Val14-RhoA (donated by Dr. A. Hall) was loaded with 1 mM GTP at 37°C for 90 min. Ten micrograms of Citron, Rhotekin, or ROCK GST-RBD conjugated with glutathione beads was mixed with 5 μg of GTP-Val14-RhoA in 50 μl of 50 mM Tris-HCl (pH 7.4), 5 mM $MgCl_2$, 0.5 mM GTP, 2 mg/ml BSA (binding buffer). Binding was for 60 min at 10°C. The beads were washed twice with binding buffer and subjected to SDS-polyacrylamide gel electrophoresis on a 12% gel. RhoA background binding to glutathione beads was negligible. In the case of experiments in the presence of P1-RhoA peptides, the regions were previously dissolved in binding buffer at 1 mg/ml.

RhoA activation by CCL21 was evaluated by using the rho binding region (RBD) from Rhotekin. Lymphocytes were lysed on ice in 0.5 ml of 100 mM HEPES buffer (pH 7.5), 1% Triton X-100, 1% deoxycholate, 0.1% SDS, 500 mM NaCl, 10 mM $MgCl_2$, 2 mM EGTA, 2 mg/ml BSA, 20 mM benzamidine, containing the Complete Protease Inhibitor Cocktail from Roche. Equal amounts of lysates were incubated with GST-RBD (20 μg) beads for 45 min at 4°C. Bound GTP-RhoA was identified by Western blotting using a monoclonal antibody from Santa Cruz.

Evaluation of Actin Stress Fibers Content

Swiss 3T3 mouse fibroblasts were maintained in DMEM containing 10% FCS for 6 days and then starved for 12 hr. Actin stress fibers content was evaluated in permeabilized cells with TRITC-labeled phalloidin as described (Ridley et al., 1992). Analysis was performed by using a Zeiss LSM confocal microscope.

NADPH-Oxidase Activation

Activation of neutrophil NADPH-oxidase was evaluated by measuring reduction of dihydrorhodamine induced by superoxide anion-derived hydrogen peroxide, as previously reported (Laudanna et al., 1998). Human neutrophils were stimulated under stirring at 37°C. Time course of hydrogen peroxide-induced dihydroRhodamine reduction was evaluated using the spectrofluorimeter with 505 of excitation wavelength and 534 of emission wavelength.

In Vitro Rapid Adhesion Assay on ICAM-1

ICAM-1 was purified from mouse spleens and adhesion assays were performed as previously reported (Constantin et al., 2000). In brief, primary naive lymphocytes (about 70% T, 30% B cells) were isolated from peripheral lymph nodes and Peyer's patches from young BALB/c mice (Harlan, Italy). Cells were resuspended at 4×10^6/ml in PBS, $CaCl_2$, $MgCl_2$ 1 mM, 10% FCS (pH 7.2). Adhesion assays were performed on 18-well glass slides coated overnight at 4°C with purified mouse ICAM-1; site density per square micrometer of immobilized ICAM-1 was calculated as reported (Lawrence and Springer, 1991). Twenty microliters of cell suspension was added to the wells and stimulated at 37°C with 5 μl of agonists prior to washing, fixation, and computer-assisted enumeration of bound cells.

Calculation of Internalization Efficiency of the Penetratin-1-RhoA Peptides

Preliminary experiments carried out with fluorescent peptides showed that P1 and P1-RhoA peptides accumulated in a comparable manner in about 95% of lymphocytes (data not shown), as also previously reported (Fenton et al., 1998). P1 and P1-RhoA peptides were labeled with ^{125}I using the Bolton-Hunter reagent (Pierce) following instructions from the manufacturer. After loading, cells were rapidly washed three times in PBS, mildly treated with trypsin to remove peptides eventually adsorbed to the outer plasma membrane (Richard et al., 2002), and the internalized radioactivity was measured with a γ counter. Treatment with trypsin removed no more than 5%–10% of total radioactivity. Specific activity was converted in CPM/molecules and then the number of molecules per cell was calculated. Loading efficiency at room temperature or 37°C was identical but was reduced about 40% at 4°C. Loading was linear between 10 and 150 μM. Peptide loading was detected after 30 min and reached a plateau within 4–8 hr, depending upon peptide concentration. The presence of 10% serum did not affect protein loading.

Measurement of LFA-1 High-Affinity State

Induction of LFA-1 high-affinity state by CCL21 was evaluated by measuring binding of soluble ^{125}I-ICAM-1, as we previously described (Constantin et al., 2000). In brief, ICAM-1 was iodinated with ^{125}NaI by the Chizzonite method. The binding assay was performed at 37°C in a 500 μl Eppendorf tube. Forty microliters of lymphocyte suspension (5×10^7/ml in PBS containing 1 mg/ml BSA, 2 mM $MgCl_2$, 1 mM $CaCl_2$, 1 mM D-glucose [pH 7.2]) was directly layered on 100 μl oil cushion of 2/1 dibutyl/dioctyl phthalates. Lymphocytes were stimulated with 10 μl of PBS containing chemokine (6 μM) and ^{125}I-ICAM-1 (5×10^5 CPM corresponding approximately to 2 μg of ^{125}I-ICAM-1). The binding reaction was stopped by rapid centrifugation in microfuge. Radioactivity bound to lymphocytes was counted with a γ counter.

Evaluation of LFA-1 Distribution on Plasma Membrane

Analysis and quantification of chemokine-induced LFA-1 surface distribution was determined by confocal microscopy, following the same procedure previously described (Constantin et al., 2000). In brief, lymphocytes were stimulated in suspension under stirring and then immediately fixed in 1% ice-cold paraformaldehyde in PBS (pH 7.4) for 10 min. Cell were washed and incubated with 10 μg/ml of TIB213 rat anti-mouse LFA-1 (ATCC) for 30 min on ice, washed three times and then incubated 30 min with Texas red-conjugated goat anti-rat secondary antibody. The washed cells adhered for 30 min at 4°C on 0.1% poly-L-lysine coated round 13 mm glass coverslips and were analyzed with a Carl Zeiss LSM 510 confocal imaging system, with a 63× C-Apochromat objective (NA 1.2). Definition and quantitative analysis of "disperse" and "clustered" morphologies of LFA-1 distribution was as previously described (Constantin et al., 2000).

Measurement of ζ PKC Kinase Activity

The assay was performed as previously described (Laudanna et al., 1998). In brief, lymphocytes were stimulated under stirring with agonists at 37°C. Stimulation was stopped with lysis buffer containing 50 mM Tris-HCl (pH 7.5), 1% Triton X-100, 0.01% SDS, 150 mM NaCl, 50 mM NaF, 10 mM sodium pyrophosphate, 1 μM phenylarsine oxide, containing the Complete Protease Inhibitor Cocktail from Roche. After 30 min on ice, lysates were centrifuged at 16,000 g for 1 min to remove cell debris. Rabbit polyclonal anti-ζ PKC (1 μg) or control rabbit serum was added to an equal amount of cell lysates, followed by immunoprecipitation with trisacryl protein A. Equal amounts of ζ PKC were immunoprecipitated as confirmed by Western blot analysis (data not shown). After four washings, immunoprecipitates were subjected to the kinase reaction for 30 min at 30°C in 50 μl of kinase buffer containing 0.5 mM EGTA, 10 mM MgC_2, 20 mM HEPES (pH 7.4), 50 μM ATP, 5 μCi [γ-^{32}P]ATP, and 2 μg myelin basic protein (MBP) as a substrate. The reaction was stopped by addition of 5% TCA, and the reaction mixture was filtered through phosphocellulose paper. After four rinses with 1% phosphoric acid radioactivity on the filter was determined with a scintillation counter.

Evaluation of ζ PKC Evaluation of Intracellular Distribution

The assay was performed as previously described (Laudanna et al., 1998). In brief, lymphocytes were stimulated under stirring with agonists at 37°C. Stimulation was stopped by diluting the cells in a 10× larger volume of ice-cold PBS. Cells, resuspended in 1 ml of ice-cold PBS containing 8% sucrose, containing the Complete Protease Inhibitor Cocktail from Roche, were sonicated, and the homogenates were centrifuged at 800 × g/10 min to remove nuclei and unbroken cells. The postnuclear supernatant was loaded on discontinuous sucrose gradient (50% sucrose, 30% sucrose) and centrifuged for 120 min at 100,000 × g. The light membrane fraction (plasma membrane) was collected in the 30% layer. Following SDS-PAGE on 10% acrylamide, proteins were electroblotted on nitrocellulose filters, probed with rabbit polyclonal antibodies anti ζ PKC

(Santa Cruz Biotechnology), followed by goat polyclonal anti-rabbit HRP conjugated (Sigma), and developed using ECL (Amersham).

Intravital Video Microscopy Analysis of Lymphocyte-High Endothelial Venule Interaction in Peyer's Patches

Lymphocytes (5×10^6/ml in DMEM without sodium bicarbonate supplemented with 20 mM HEPES, 5% FCS (pH 7.1) were labeled with either CMFDA or CMTMR for 30 min at 37°C. 30×10^6 labeled cells were injected iv. In situ videomicroscopic analyses were carried out in high endothelial venules (HEV) in the secondary lymphoid organ Peyer's patch as described (Constantin et al., 2000). Cell behavior was analyzed over a period of 20–30 min starting at 2 min after iv injection. Interactions of ≥1 s were considered significant and were scored. Cells were considered to be interacting whether they rolled, arrested, or both. Lymphocytes that remained firmly adherent on venular wall for ≥10 s were considered arrested.

Acknowledgments

This work was supported by Fondazione Cassa di Risparmio, by a grant from Italian Association for Cancer Research (AIRC) 2002, by Italian Ministry of Health (RF. 00177; 0095; 00103) Fondo Incentivazione Ricerca di Base (FIRB), by Fondazione Italiana Sclerosi Multipla (FISM) (2000/R/71), and by NIH grant GM37734 (to E.C.B.). We thank Professor G. Fumagalli for providing the confocal microscopy facility.

Received: May 5, 2003
Revised: November 5, 2003
Accepted: November 11, 2003
Published: January 20, 2004

References

Abo, A., Pick, E., Hall, A., Teahan, C.G., and Segal, A.W. (1991). Activation of the NADPH oxidase involves the small GTP-binding protein $p21^{rac1}$. Nature *353*, 668–670.

Amano, M., Chihara, K., Kimura, K., Fukata, Y., Nakamura, N., Matsura, Y., and Kaibuchi, K. (1997). Formation of actin stress fibers and focal adhesions enhanced by Rho-kinase. Science *275*, 1308–1311.

Constantin, G., Majeed, M., Giagulli, C., Piccio, L., Kim, J.Y., Butcher, E.C., and Laudanna, C. (2000). Chemokines trigger immediate β2 integrin affinity and mobility changes: differential regulation and roles in lymphocyte arrest under flow. Immunity *13*, 759–769.

Dae Bae, C., Sik Min, D., Fleming, I.N., and Exton, J.H. (1998). Determination of interaction sites on the small G protein RhoA for phospholipase D. J. Biol. Chem. *273*, 11596–11604.

Fenton, M., Bone, N., and Sinclair, A.J. (1998). The efficient and rapid import of a peptide into primary B and T lymphocytes and a lymphoblastoid cell line. J. Immunol. Methods *212*, 41–48.

Fujisawa, K., Madaule, P., Ishikazi, T., Watanabe, G., Bito, H., Saito, Y., Hall, A., and Narumiya, S. (1998). Different regions of Rho determine Rho-selective binding of different classes of Rho target molecules. J. Biol. Chem. *273*, 18943–18949.

Kimura, K., Tsuji, T., Takada, Y., Miki, T., and Narumiya, S. (2000). Accumulation of GTP-bound RhoA during cytokinesis and a critical role of ECT2 in this accumulation. J. Biol. Chem. *275*, 17233–17236.

Kunkel, E.J., and Butcher, E.C. (2002). Chemokines and the tissue-specific migration of lymphocytes. Immunity *16*, 1–4.

Laudanna, C., Campbell, J.J., and Butcher, E.C. (1996). Role of Rho in chemoattractant-activated leukocyte adhesion through integrins. Science *271*, 981–983.

Laudanna, C., Mochly-Rosen, D., Liron, T., Constantin, G., and Butcher, E.C. (1998). Evidence of ζ protein kinase C involvement in polymorphonuclear neutrophil integrin-dependent adhesion and chemotaxis. J. Biol. Chem. *273*, 30306–30315.

Laudanna, C., Kim, J.Y., Constantin, G., and Butcher, E.C. (2002). Rapid leukocyte integrin activation by chemokines. Immunol. Rev. *186*, 37–46.

Lawrence, M.B., and Springer, T.A. (1991). Leukocytes roll on a selectin at physiologic flow rates: distinction from and prerequisite for adhesion through integrins. Cell *65*, 859–873.

Le Good, J.A., Ziegler, W.H., Parekh, D.B., Alessi, D.R., Cohen, P., and Parker, P.J. (1998). Protein kinase C isotypes controlled by phosphoinositide 3-kinase trough the protein kinase PDK1. Science *281*, 2042–2045.

Limatola, C., Barabino, B., Nista, A., and Santoni, A. (1997). Interleukin 1-β-induced protein kinase C-ζ activation is mimicked by exogenous phospholipase D. Biochem. J. *321*, 497–501.

Nagel, W., Zeiltmann, L., Schilcher, P., Gieger, C., Kolanus, J., and Kolanus, W. (1998). Phosphoinositide 3-OH kinase activates the β2 integrin adhesion pathway and induces membrane recruitment of cytohesin-1. J. Biol. Chem. *273*, 14853–14861.

Prochiantz, A. (2000). Messenger proteins: homeoproteins, TAT and others. Curr. Opin. Cell Biol. *12*, 400–407.

Ren, X.-D., Kiosses, W.B., and Schwartz, M.A. (1999). Regulation of the small GTP-binding protein Rho by cell adhesion and the cytoskeleton. EMBO J. *18*, 578–585.

Richard, J.P., Melikov, K., Vives, E., Ramos, C., Verbeure, B., Gait, M.J., Chernomordik, L.V., and Lebleu, B. (2002). Cell penetrating peptides: a reevaluation of the mechanism of cellular uptake. J. Biol. Chem. *278*, 585–590.

Ridley, A.J., and Hall, A. (1992). The small GTP-binding protein rho regulates the assembly of focal adhesions and actin stress fibers in response to growth factors. Cell *70*, 389–399.

Ridley, A.J., Paterson, H.F., Johnston, C.L., Diekmann, D., and Hall, A. (1992). The small GTP-binding protein *rac* regulates growth factor-induced membrane ruffling. Cell *70*, 401–410.

Shimonaka, M., Katagiri, K., Nakayama, T., Fujita, N., Tsuruo, T., Yoshie, O., and Kinashi, T. (2003). Rap1 translates chemokine signals to integrin activation, cell polarization, and motility across vascular endothelium under flow. J. Cell Biol. *161*, 417–427.

Slater, S.J., Seiz, J.L., Stagliano, B.A., and Stubbs, C.D. (2001). Interaction of protein kinase C isozymes with Rho GTPases. Biochemistry *40*, 4437–4445.

Stokoe, D., Macdonald, S.G., Cadwallader, K., Symon, M., and Hancock J.F. (1994). Activation of raf as a result of recruitment to the plasma membrane. Science *264*, 1463–1467.

Uehata, M., Ishizaki, T., Satoh, H., Ono, T., Kawahara, T., Morishita, T., Tamakawa, H., Yamagami, K., Inui, J., Maekawa, M., and Narumiya, S. (1997). Calcium sensitization of smooth muscle mediated by a Rho-associated protein kinase in hypertension. Nature *389*, 990–994.

Warnock, R.A., Campbell, J.J., Dorf, M.E., Matsuzawa, A., McEvoy, L.M., and Butcher, E.C. (2000). The role of chemokines in the microenvironmental control of T versus B cell arrest in Peyer's patch high endothelial venules. J. Exp. Med. *191*, 77–88.

Weber, K.S., Weber, C., Ostermann, G., Dierks, H., Nagel, W., and Kolanus, W. (2001a). Cytohesin-1 is a dynamic regulator of distinct LFA-1 functions in leukocyte arrest and transmigration triggered by chemokines. Curr. Biol. *11*, 1969–1974.

Weber, K.S., Ostermann, G., Zemeche, A., Schroder, A., Klickstein, L.B., and Weber, C. (2001b). Dual role of H-Ras in regulation of lymphocyte function antigen-1 activity by stromal cell-derived factor-1alpha: implications for leukocyte transmigration. Mol. Biol. Cell *12*, 3074–3086.

Molecular Cell, Vol. 13, 511–522, February 27, 2004, Copyright ©2004 by Cell Press

The Core FH2 Domain of Diaphanous-Related Formins Is an Elongated Actin Binding Protein that Inhibits Polymerization

Atsushi Shimada,[1,6] Miklós Nyitrai,[2,3,6] Ingrid R. Vetter,[1] Dorothee Kühlmann,[1] Beáta Bugyi,[4] Shuh Narumiya,[5] Michael A. Geeves,[2] and Alfred Wittinghofer[1,*]
[1]Max-Planck Institut für Molekulare Physiologie
Otto Hahn Strasse 11
D-44227 Dortmund
Germany
[2]Department of Biosciences
University of Kent
Canterbury, Kent CT2 7NJ
United Kingdom
[3]Research Group for Fluorescence Spectroscopy
Office for Academy Research Groups Attached to Universities and Other Institutions
[4]Department of Biophysics
Faculty of Medicine
University of Pécs
H-7601 Pécs
Hungary
[5]Department of Pharmacology
Kyoto University Faculty of Medicine
Yoshida, Sakyo-ku, Kyoto 606-8501
Japan

Summary

Diaphanous-related formins (Drf) are activated by Rho GTP binding proteins and induce polymerization of unbranched actin filaments. They contain three formin homology domains. Evidence as to the effect of formins on actin polymerization were obtained using FH2/FH1 constructs of various length from different Drfs. Here we define the core FH2 domain as a proteolytically stable domain of approximately 338 residues. The monomeric FH2 domains from mDia1 and mDia3 inhibit polymerization of actin and can bind in a 1:1 complex with F-actin at micromolar concentrations. The X-ray structure analysis of the domain shows an elongated, crescent-shaped molecule consisting of three helical subdomains. The most highly conserved regions of the domain span a distance of 75 Å and are both required for barbed-end inhibition. A construct containing an additional 72 residue linker has dramatically different properties: It oligomerizes and induces actin polymerization at subnanomolar concentration.

Introduction

The formin proteins play important roles in many different cellular processes such as cytokinesis, vesicular trafficking, and the maintenance of cell polarity by regulating actin and microtubule cytoskeletons (Wallar and Alberts, 2003). They have in common a poly-proline-rich formin homology-1 (FH1) domain, which binds profilin and protein-interacting modules such as the SH3 or WW domain (Wallar and Alberts, 2003). They also contain a FH2 domain of undefined length and structure, usually in tandem with FH1.

Diaphanous-related formins (Drfs) such as the (mammalian) mDia proteins (mDia 1, 2, and 3) have an additional GTPase binding domain (GBD) which is involved in binding the GTP-bound form of Rho proteins (Evangelista et al., 1997; Kohno et al., 1996; Watanabe et al., 1997), connected to the FH3 domain of undefined length and structure. In Drfs the activity of the protein is regulated by the C-terminal diaphanous autoregulatory domain (DAD), which binds to the GBD and inhibits biological activity (Watanabe et al., 1999; Alberts, 2001). While mDia is directly mediating Rho-induced actin reorganization (Watanabe et al., 1997, 1999), it has also been implicated in microtubule alignment and stabilization (Ishizaki et al., 2001; Palazzo et al., 2001).

It has been shown that the FH2 domain plays an important role for the function of formin family proteins. Mutations in the FH2 domain abolish both the bundling of actin filaments and the alignment of microtubules induced by an active mutant of mDia1 lacking the GBD (Ishizaki et al., 2001). A close link exists between the control of cytoskeletal organization and the transcription factor serum response factor (SRF), where SRF is negatively regulated by the actin monomer pool in the cells (Posern et al., 2002; Sotiropoulos et al., 1999). For this system it has been shown in cell culture studies that the lysophosphatidic acid (LPA)-induced activation of SRF is mediated by mDia and in particular by the region encompassing the FH2 domains (Copeland and Treisman, 2002).

Fragments of various length covering the FH2 domains of formins exhibited activity to nucleate actin in vitro (Pruyne et al., 2002; Sagot et al., 2002b; Pring et al., 2003; Kovar et al., 2003; Li and Higgs, 2003). All the FH2 fragments from either *S. cerevisiae* Bni1p, *S. pombe* Cdc12p, or mDia1 used in the previous studies (Figure 1A) have in common the property to affect barbed-end kinetics of F-actin via a complete or partial capping mechanism. Although the FH1 domain is dispensable for in vitro actin polymerization induced by the FH2 domain, it modulates the activity of the FH2 domain by its interaction with profilin (Pruyne et al., 2002; Sagot et al., 2002b; Kovar et al., 2003; Li and Higgs, 2003). It has been also proposed that these fragments form a dimer or higher oligomers, which is likely related to their function (Li and Higgs, 2003; Zigmond et al., 2003; Takeya and Sumimoto, 2003).

The exact domain boundaries of the FH2 domain and the minimal functional unit for actin nucleation were not clear. To dissect and structurally define the domain boundaries of these proteins and to understand the contribution of the core FH2 domain (as defined in this article) to actin polymerization, we isolated and characterized proteolytically stable FH2 domain fragments from both mouse mDia1 and mDia3. The 338 residue fragment did not nucleate, but did inhibit, actin polymerization. We also show that the additional presence of the linker region between the FH1 and FH2 domain is

*Correspondence: alfred.wittinghofer@mpi-dortmund.mpg.de
[6]These authors contributed equally to this work.

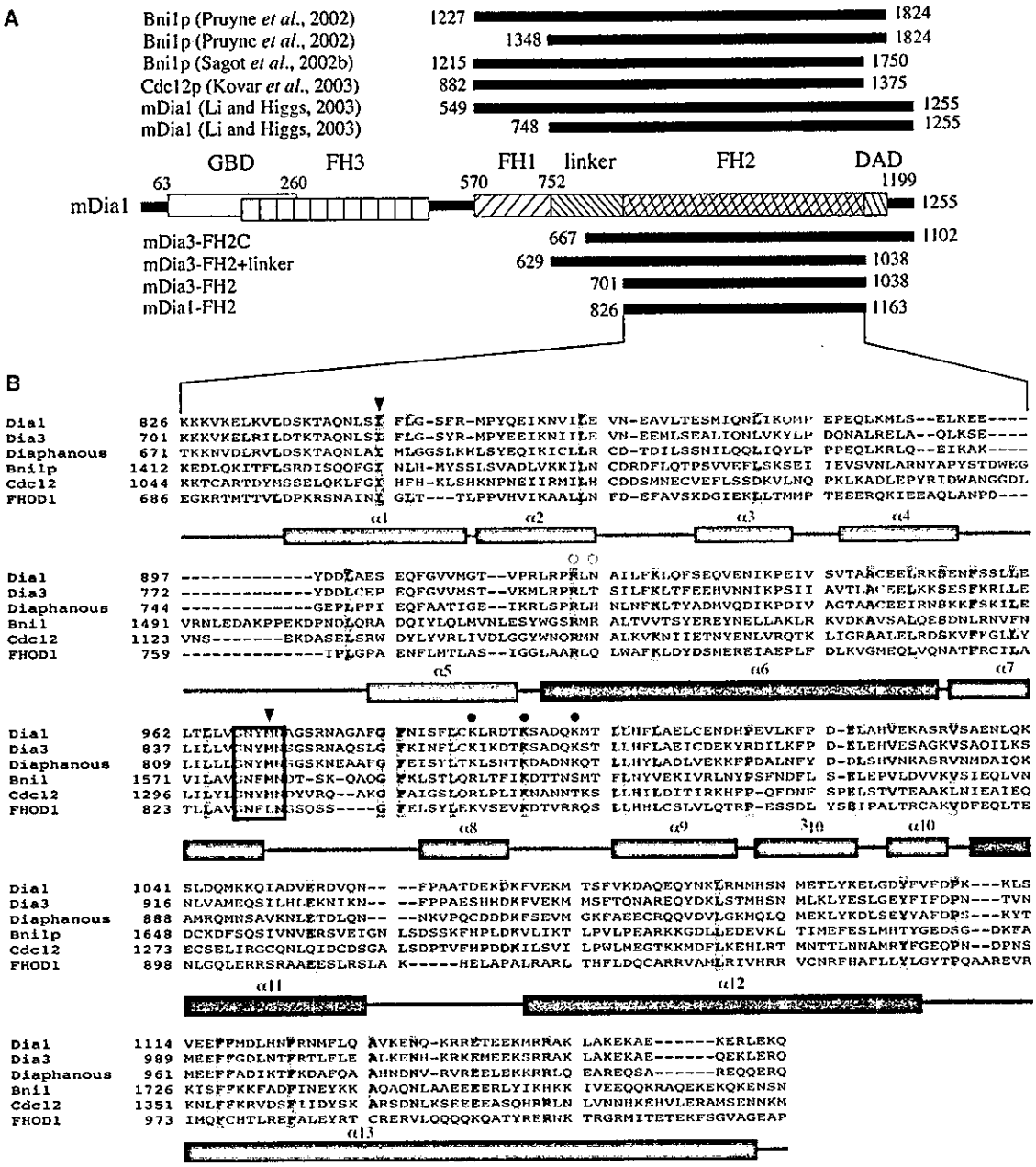
A
Bni1p (Pruyne et al., 2002)
Bni1p (Pruyne et al., 2002)
Bni1p (Sagot et al., 2002b)
Cdc12p (Kovar et al., 2003)
mDia1 (Li and Higgs, 2003)
mDia1 (Li and Higgs, 2003)
GBD
FH3
FH1
linker
FH2
DAD
mDia1
mDia3-FH2C
mDia3-FH2+linker
mDia3-FH2
mDia1-FH2
B
Dia1
Dia3
Diaphanous
Bni1p
Cdc12
FHOD1
α1
α2
α3
α4
α5
α6
α7
α8
α9
α10
α11
α12
α13
C
50.8 kDa, mDia3-FH2C (667-1102)
% Intensity
Mass (m/z)

necessary for the core FH2 domain to form oligomers and to induce actin polymerization. The structure of the FH2 domain of mouse mDia1 was determined at a resolution of 2.6 Å. The structure exhibited an exclusively helical fold distinct from other known F-actin binding folds and provided implications for the mechanism of formin-mediated actin polymerization.

Results

Identification of a Stable mDia FH2 Core Domain

Initial trials of expression of two FH2 domain constructs from mouse mDia3 (mDia3-FH2N [residues 629–1037] and mDia3-FH2C [residues 667–1102]) were unsuccessful due to their insolubility. Although mDia3-FH2C was partly expressed as a soluble protein and copurified with chaperone, it was unstable and produced several degradation products after purification on a GSH-column (Figure 1C). The mDia3-FH2C was further degraded at 37°C for 5 days to produce a stable 40 kDa fragment (Figure 1; residues 701–1038). Proteolytic digestion of mDia3-FH2C by trypsin and α-chymotrypsin produced fragments of similar or slightly smaller size, indicating that the 40 kDa fragment delineates the FH2 domain. The domain boundaries of the stable fragment were deduced from mass analyses. The corresponding 40 kDa fragments (338 amino acids) from mDia1 or mDia3, and a fragment having in addition to the mDia3-FH2 the linker region between the FH1 and the core FH2 (residues 629–1038) could be stably expressed in large amounts as *E. coli* recombinant proteins.

The Interaction of the Core FH2 Domain with Actin

In preliminary experiments, where the actin was polymerized with 100 mM KCl and 2 mM $MgCl_2$, the effect of 10 μM FH2 was very weak (<5%) due to the relatively high ionic strength (data not shown). To increase the affinity of formin for actin, we used low salt conditions in the assays (see Experimental Procedures). The presence of micromolar concentrations of the core mDia1-FH2 or mDia3-FH2 domains decreased the rate of spontaneous actin polymerization (3.5 μM, 5% pyrene-labeled; Figure 2A). The elongation rates were estimated from the slopes of the normalized pyrene transients at 50% completion of the reaction (insert in Figure 2A). Hyperbola fits to the [FH2] dependence of the elongation rate showed that at saturating [mDia1-FH2] or [mDia3-FH2] the elongation rate decreased to 41 ± 3% or to 26 ± 2% of the value measured in the absence of FH2. Half saturation concentrations were 1.96 ± 0.43 μM and 2.05 ± 0.22 μM, respectively.

The depolymerization rates of actin filaments were measured by diluting actin filaments (5 μM, 68% pyrene-labeled) to 0.1 μM into polymerization buffer alone, or supplemented with mDia1-FH2 or mDia3-FH2. The actin monomer dissociation rates were estimated from the initial slopes of the pyrene transients (first 50 s, Figure 2B) as described in Li and Higgs (2003). The determined rates were plotted as a function of [FH2] and at saturation hyperbolae fits gave 44 ± 6% and 1 ± 4% of the rates measured in the absence of FH2 for mDia1-FH2 and mDia3-FH2, respectively (insert in Figure 2B). Half saturation concentrations were 1.89 ± 0.76 μM and 1.31 ± 0.26 μM, respectively. The effect of mDia1-FH2 on the depolymerization rate of actin filaments (Figure 2B) was similar to the observation that mDia1(549–1255) (involving the FH1 and FH2 domains) decreased the depolymerization rate of actin to ~50% (Li and Higgs, 2003). The difference between the two sets of results is that the effect of mDia1(549–1255) saturated below 50 nM, while mDia1-FH2 in this study saturated at about 2 μM suggesting that the affinity of mDia1-FH2 is much weaker for actin than that of mDia1(549–1255).

The critical concentration of actin was measured in the presence and absence of a series of mDia1-FH2 or mDia3-FH2 concentrations (see Experimental Procedures). The fit to the linear part of the measured fluorescence intensity versus [actin] curves showed that either FH2 fragment increased the critical concentration (Figure 2C). mDia3-FH2 increased the critical concentration of actin from 0.23 μM to ~1 μM (insert in Figure 2C) while the effect of mDia1-FH2 was smaller, increasing the critical concentration to 0.4 μM (insert in Figure 2C). The mDia1-FH2 fragment decreased the elongation rate to ~41% (Figure 2A) and the depolymerization rate to ~44% (Figure 2B), which is consistent with the small mDia1-FH2-induced change of the critical concentration (Figure 2C). In the case of mDia3-FH2 the effect on the dissociation rate was stronger (decreased to <5%) (Figure 2B) while the elongation rate decreased to 26% (Figure 2A), suggesting a decrease in the critical concentration. In contrast with expectation, the critical concentration increased in the presence of mDia3-FH2 (Figure 2C), suggesting that more detailed experimental analysis is required to clarify this discrepancy.

Figure 1. Domain Organization and Primary and Secondary Structure Alignment of the Core FH2 Domain from mDia1

(A) The middle part shows locations of GTPase binding domain (GBD), formin homology domains 1 (FH1), 2 (FH2), and 3 (FH3), linker, and diaphanous autoregulatory domain (DAD) of mDia1. Numbers denote residue number. Fragments used in previous biochemical studies and their location and size relative to mDia1 are indicated above. Fragments of mDia1 and mDia3 used in the present study and their respective length are shown below.

(B) The amino acid sequence of the core FH2 domain of mDia1 (mouse) is compared with those of mDia3 (mouse), Diaphanous (*Drosophila*), Bni1p (*S. cerevisiae*), Cdc12p (*S. pombe*), and FHOD1 (human). Amino acid residues conserved in all the six aligned formin family proteins are colored orange, whereas those conserved in five out of six proteins are colored yellow. An open box indicates the location of the highly conserved G-N-X-M-N motif. Arrowheads indicate positions of mutated residues Ile845 and Met970. Filled circles indicate positions of three Lys residues whose replacement with Ala abolished alignment of microtubules and bundling of F-actin (see text). Open circles indicate residues replaced in Bni1p temperature-sensitive mutants (see text). Secondary structure elements of the FH2 domain obtained from the structure determination are indicated below the amino acid sequence. Regions corresponding to the NH_2-terminal, three-helix-bundle, and the FH2 motif subdomains are colored red, blue, and green, respectively.

(C) SDS gel showing the degradation of the mDia3 FH2C (top) and the corresponding mass spectrometric analysis (bottom). Masses were obtained from MALDI-TOF-MS.

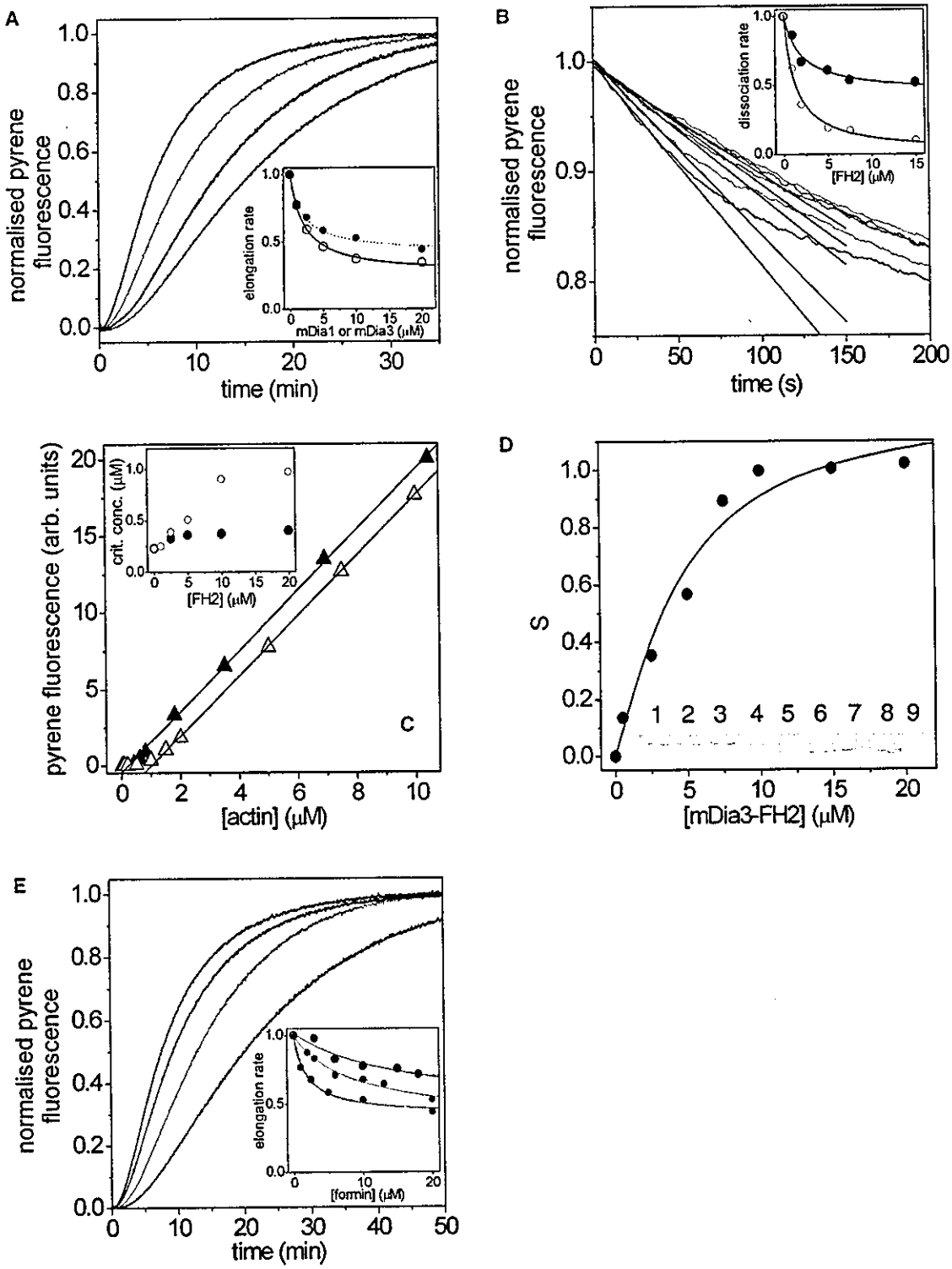

Figure 2. Biochemical Analysis of the Core FH2 Domain

(A) Polymerization. Actin monomers (3.5 μM, 5% pyrene-labeled) were polymerized in the absence or presence of FH2 fragments, and the pyrene fluorescence was monitored. The figure shows the normalized pyrene fluorescence transients obtained at different [mDia1-FH2] (0 μM [black], 2.5 μM [red], 5 μM [green], and 10 μM [blue]). Similar experiments were carried out with mDia3-FH2 as well (traces are not shown). The insert shows the relative elongation rate (estimated from the slopes at 50% saturation) as a function of [mDia1-FH2] (filled circles) or of [mDia3-FH2] (empty circles). Hyperbola fits to the mDia1-FH2 (dashed line) data and to the mDia3-FH2 (solid line) data are superimposed.

(B) Depolymerization. Actin (5 μM, 68% pyrene-labeled) was polymerized and diluted to 0.1 μM into polymerization buffer alone or to polymerization buffer supplemented with FH2. The figure shows the normalized fluorescence transients measured at different [mDia1-FH2] (0 μM [black], 1 μM [red], 2 μM [green], 5 μM [blue], and 7 μM [magenta]). Linear fits to the first 50 s are shown as solid lines. Similar experiments were carried out with mDia3-FH2 as well (traces are not shown). The insert shows the relative dissociation rate (slope of the

It was shown that the mDia1(549–1255) fragment involving the FH1, linker, FH2, DAD, and C terminus can bind to preformed actin filaments (Li and Higgs, 2003). To test whether our FH2 fragments retain this ability, we estimated the affinity of FH2 for actin filaments in cosedimentation assays (see Experimental Procedures). Polyacrylamide gel analysis shows (Figure 2D) that mDia3-FH2 (lower band) is cosedimented with preformed actin filaments (upper band) in a 1:1 complex with actin protomer. Due to the fraction of actin below the critical concentration, some actin remained in the supernatant, the amount of which increased by a factor of ~3 at [mDia3-FH2] >10 μM relative to that in the absence of mDia3 FH2 (insert in Figure 2D), consistent with mDia3-FH2-induced increase of the critical concentration (Figure 2C). Lane 9 shows that excess mDia3-FH2 in the absence of actin does not precipitate. The analysis of the gels (Equation 1) gave a K_D of 2.9 ± 1.2 μM for mDia3-FH2 binding to F-actin (Figure 2D). mDia1-FH2 also bound to actin filaments but the S versus [mDia1-FH2] plot (see Experimental Procedures) did not saturate below 20 μM mDia1-FH2 (data not shown), suggesting that the binding was weaker.

The mDia1(549–1255) fragment bound preformed actin filaments with an apparent K_D of 3 μM (Li and Higgs, 2003). Our result with mDia3-FH2 (2.9 ± 1.2 μM, Figure 2D) was close to the value obtained with mDia1(549–1255). Although we used lower salt conditions, the affinity of mDia1-FH2 in our experiments was weaker than that of mDia1(549–1255) (Li and Higgs, 2003), indicating that regions outside the FH2 domain contribute to the binding of mDia1 to preformed actin filaments. The half saturation of the effects of both mDia1-FH2 and mDia3-FH2 on the elongation or depolymerization was between 1 and 2 μM (Figures 2A and 2B). The affinity of mDia3-FH2 for actin filaments is close to this concentration range, but the affinity of mDia1-FH2 for actin is much weaker. For mDia1(549–1255) the K_D for the affinity to actin filaments was 3 μM, while the effect of mDia1(549–1255) on the kinetics parameters was in the nanomolar range. All these points to the conclusion, that there is no obvious correlation between the affinity of the formin fragments for preformed actin filaments and their effect on the polymerization of actin.

Overall Structure of the Core FH2 Domain of mDia1

The crystal structure of the mDia1-FH2 (338 amino acid residues, 40 kDa) was determined at 2.6 Å resolution (Table 1). The asymmetric unit of the crystal contained four molecules, denoted A, B, C, and D (Figure 3A). The present model contains residues 829–960 and 985–1160 of molecule A, residues 830–1150 of molecule B, residues 829–952, 955–962, and 1000–1150 of molecule C, and residues 830–963 and 985–1150 of molecule D. The other parts of the molecules had poor or uninterpretable electron densities and could not be modeled. The missing residues are located either at the N terminus, C terminus, or in a region covering the conserved FH2 motif of approximately 70 residues (see below). The electron densities for the region covering the FH2 motif were best defined for the molecule B probably due to crystal packing, and a representative example of the map is shown in Figure 3B. Since the visible parts are very similar in the four molecules, besides some hinge-bending movement of molecules A/C compared to B/D (see below), we will hereafter describe the structure of the FH2 domain based on molecule B unless mentioned otherwise.

The FH2 domain is an elongated crescent-shaped molecule with an approximate size of 100 Å by 25 Å by 25 Å composed exclusively of α helices (Figure 4A). The structure of the FH2 domain can be divided into three subdomains: the NH_2-terminal subdomain (red), the three-helix-bundle subdomain (blue), and the FH2 motif (green) because the latter encompasses the region originally defined and still documented as FH2 (Castrillon and Wasserman, 1994; Watanabe et al., 1997; Wallar and Alberts, 2003).

The Subdomains

The NH_2-terminal subdomain (84 aa) is composed of five α helices. DALI search (Holm and Sander, 1994) found six proteins as structural homologs. However, the Z scores between the NH_2-terminal subdomain and those proteins are low (Z < 2.4). From the low similarity, it seems unlikely that there are any functional or evolutionary connections between them.

The three-helix-bundle subdomain is composed of three antiparallel α helices, which form a left-handed coiled-coil structure. DALI search found a number of structural homologs, such as syntaxin1a (Z = 9.5, PDB code 1br0) (Fernandez et al., 1998), Smac/DIABLO (Z = 8.6, PDB code 1few) (Chai et al., 2000), spectrin-repeats of spectrin (Z = 8.6, PDB code 1cun) (Grum et al., 1999), and α-actinin (Z = 8.0, PDB code 1quu) (Djinovic-Carugo et al., 1999). Most of these proteins have three- or four-

linear fits) as a function of [mDia1-FH2] (filled circles) or [mDia3-FH2] (empty circles). Hyperbola fits to the data are shown as solid lines.

(C) Effect on the critical concentration of actin assembly. Actin (5% pyrene-labeled) was incubated overnight at different concentration in polymerization buffer alone or in the presence of mDia1-FH2 or mDia3-FH2. The formin concentrations were 0, 1, 2.5, 5, 10, and 20 μM. The figure shows the [actin] dependence of the pyrene fluorescence intensities measured in the absence of formin (filled triangles) or in the presence of 20 μM mDia3-FH2 (empty triangles). Fits to the linear part of the intensity versus [actin] curves gave critical concentrations of 230 nM in the absence of formin. The insert shows the [mDia1-FH2] (filled circles) or [mDia3-FH2] (empty circles) dependence of the critical concentration.

(D) Affinity for F-actin. Fraction of mDia3-FH2 bound to F-actin (S) calculated from the results of SDS-PAGE analysis of a cosedimentation assay. The analysis with Equation 1 (solid line, see Experimental Procedures) gave an apparent K_D = 2.9 ± 1.2 μM. The insert shows the gel (12.5%) of the pellet, obtained with [actin] = 3 μM and [mDia3-FH2] of 0, 0.5, 2.5, 5, 7.5, 10, 15, and 20 μM (lanes 1–8). Lane 9 is obtained with 5 μM mDia3 FH2 in the absence of actin.

(E) Mutational analysis. Normalized pyrene fluorescence transients obtained when 3.5 μM actin (5% pyrene-labeled) was polymerized in the absence of formin (black) or in the presence of 10 μM I845R (blue), 10 μM M970R (red), or 10 μM wild-type mDia1-FH2 (green). The insert shows the formin dependence of the relative elongation rates (estimated from the slopes at 50% saturation) for I845R (blue circles), M970R (red circles), and wild-type mDia1-FH2 (green). The mDia1-FH2 data are taken from (A); hyperbola fits are superimposed as solid lines.

Table 1. Data Collection, Phasing, and Refinement Statistics

	Native	SeMet
Diffraction Data		
Temperature (K)	100	100
Space group	$P2_12_12_1$	$P2_12_12_1$
Unit-cell parameters (Å)		
a	82.43	82.47
b	124.52	119.78
c	229.40	246.41
Wavelength (Å)	0.9340	0.9786
Resolution (Å)	50.0–2.6	50.0–3.4
Unique reflections	73,264	34,362
Total reflections	406,569	491,435
I/σ	18.8 (5.4)	28.4 (9.4)
R_{merge}[a]	9.9 (49.5)	10.2 (49.0)
Completeness (%)	99.6 (99.9)	99.7 (100.0)
Phasing Statistics		
Number of sites		52
Phasing power		
Anomalous (acentrics)		2.516
R_{cullis}[b]		
Anomalous (acentrics)		0.6125
Mean overall figure of merit		
Acentric		0.5248
Centric		0.2569
Refinement Statistics		
Protein atoms	9876	
Water oxygens	191	
Sulfate Ions	3	
R_{work}[c] (%)	22.99	
R_{free}[d] (%)	26.68	
Rms deviation from ideal values		
Bond length, Å	0.0084	
Bond angles, degrees	1.12	
Improper angles, degrees	0.74	
Average B factor, Å^2		
Molecule A	64.0	
Molecule B	52.8	
Molecule C	79.2	
Molecule D	90.0	
Solvent	59.4	
Sulfates	51.1	

Values in parentheses are for the highest resolution shell.
[a] $R_{merge} = \Sigma_h \Sigma_i |I_{hi} - \langle I_h \rangle| / \Sigma_h \Sigma_i |I_{hi}|$, where *h* refers to unique reflection indices and *i* indicates symmetry-equivalent indices.
[b] $R_{cullis} = \Sigma[|F_H| - (|F_{PH}| - |F_P|)]/\Sigma(|F_{PH}| - |F_P|)$, where $|F_H|$ represents the calculated heavy-atom structure factor.
[c] $R_{work} = \Sigma||F_O| - |F_C||/\Sigma|F_O|$ for the working set reflections (90% of the data) used for the refinement.
[d] $R_{free} = \Sigma||F_O| - |F_C||/\Sigma|F_O|$ for the test set reflections (10% of the data) excluded from the refinement.

helix-bundle structures. The resemblance of the FH2 domain to spectrin-repeats is particularly intriguing because spectrin-repeat-containing proteins such as spectrin and α-actinin also bind to F-actin (Grum et al., 1999; Djinovic-Carugo et al., 1999). The three-helix-bundle subdomain of FH2 and one unit of spectrin-repeats are similar in size (approximately 100 aa) and also in geometry, which is shown by an rms deviation between corresponding Cα atoms of 2.3 Å over 69 residues.

The three α helices form an extensive hydrophobic core. There is, however, a buried salt bridge between Arg919 in α6 and Asp1067 in a loop region between helices α11 and α12 (Figure 4B). These two residues are highly conserved and most likely contribute to the conformation of the loop region. In Bni1p, both Arg1528 and Arg1530 were found mutated to Ala in a temperature-sensitive mutant (Sagot et al., 2002a). Arg1528 corresponds to Arg919 of mDia1. Since replacement of Arg1528 by Ala disrupts the salt bridge, the mutation most probably destabilizes the three-helix-bundle structure and/or the interface between the three-helix-bundle and the NH_2-terminal subdomains. On the other hand, additional replacement of Arg1530 by Ala seems less important for the temperature sensitivity of Bni1p because the side chain of the corresponding Asn921 of mDia1 is exposed to solvent and seems to have no important interactions with other residues.

The FH2 motif is composed of two nonconsecutive parts of the polypeptide chains. The first segment (residues 953–1026) is located between α6 and α11 of the three-helix-bundle subdomain. It includes residues (946–1010) originally identified as FH2 (Watanabe et al., 1999) and is the evolutionary best-conserved region of the formin-family proteins (Figure 1B). The highly conserved ^{967}GNXMN^{971} motif is located at the COOH-terminal end of α7 (Figure 4A). The region around this motif is apparently very flexible, since it is only partially visible in molecules A, C, and D of the asymmetric unit. The invariant Gly967, Asn968, and highly conserved (in five of six, see Figure 1) Met970 and Asn971 seem to play structural roles where Gly967 has ϕ,ψ angles (−87, −17) not allowed for any other residue and appears to induce a particular angle of the polypeptide chain at the end of α7. Lys989, Lys994, and Lys999 are located at a tip of the FH2 motif where many conserved residues cluster (Figure 4D).

Replacement of these Lys residues by Ala abolished the alignment of microtubules and the bundling of F-actin induced by an activated mutant of mDia1 in vivo (Ishizaki et al., 2001). These Lys residues together with surrounding conserved residues may constitute the binding interface with other proteins such as F-actin. The second segment of the subdomain is formed by the long α helix (α13) and a short connecting linker. α13 sits in a cleft formed by α8, α9, a 3_{10} helix (3_{10}), α10, and connecting loops of the first segment of the subdomain.

Superimposing molecules A, C, and D on the three-helix-bundle subdomains, only the FH2 motif shows significant differences in structure between molecules B/D and A/C (Figure 4C), suggesting conformational flexibility of this region. Although only helices α9 and α13 are clearly defined in all four molecules, it appears that the FH2 motif shifts as a rigid body such that the helix α13 moves by an angle of 20°–25° relative to the three-helix-bundle subdomain (Figure 4C). It would be attractive to assume that these observed differences in structure are indicative of a conformational change that is relevant to the function of mDia1. In favor of this we note that the C-terminal helix α13 is directly linked to the autoinhibitory DAD domain whose importance for mDia regulation has been well documented (Watanabe et al., 1999; Alberts, 2001).

It was reported that an mDia1-FH2 construct encompassing residues 736–1150 induces SRF activation in vivo, which is mediated by its actin polymerization activity (Copeland and Treisman, 2002). However, C-terminal deletion of residues 1130–1150 abolished the activity of the construct for SRF activation (Copeland and Treis-

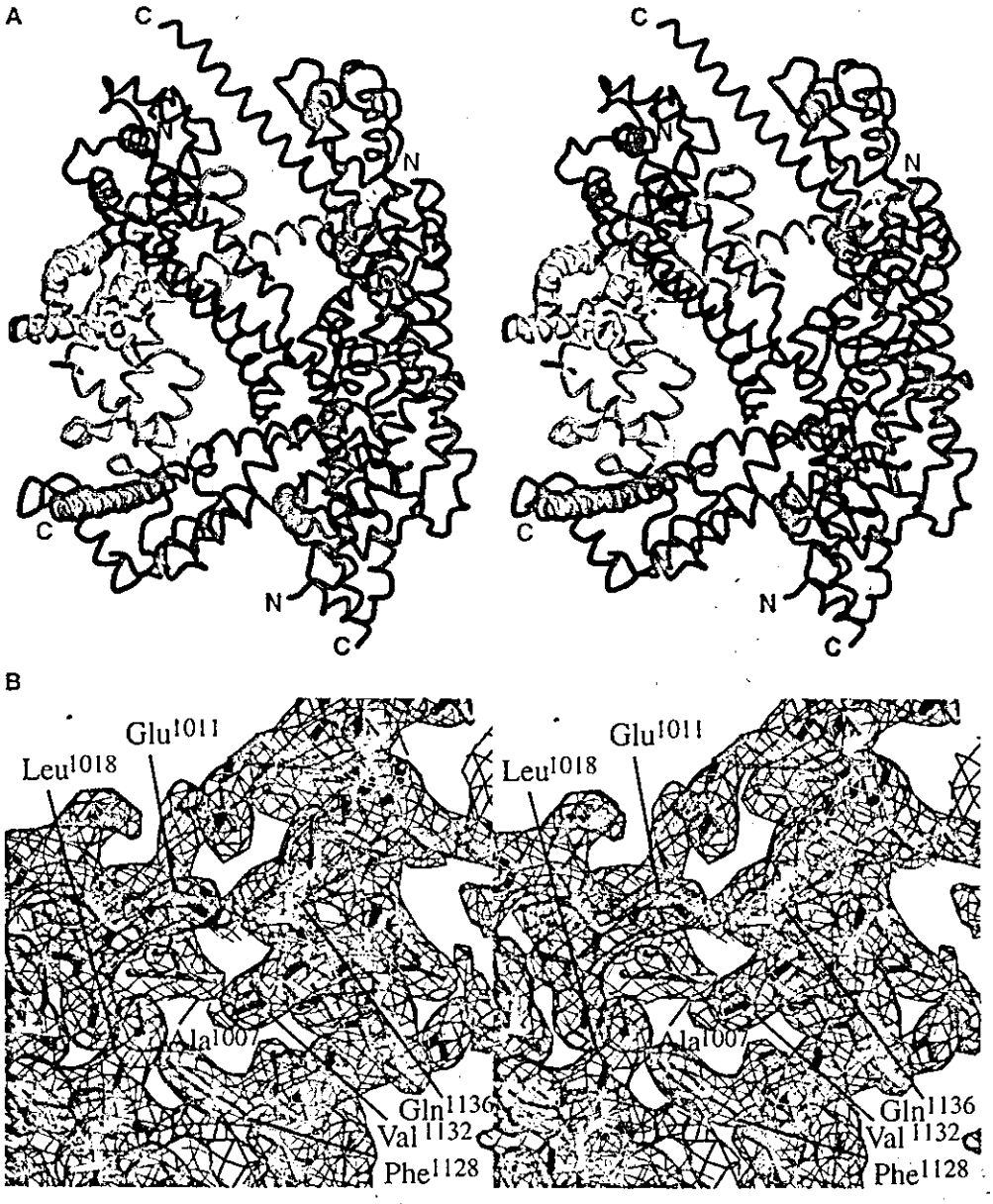

Figure 3. X-Ray Structure Solution of the Core FH2 Domain from mDia1

(A) Stereo view of the asymmetric unit. Molecules A, B, C, and D of the asymmetric unit are colored red, green, blue, and yellow, respectively, with NH_2 and COOH termini labeled correspondingly.

(B) A representative stereo electron density map. An $2F_o - F_c$ electron density map, contoured at 1.2σ, of the interface between α13 and surrounding helices α9 and 3^{10}. The residues involved in the interaction are labeled.

man, 2002). From the present structure, it is clear that the deletion of residues 1130–1150 severely disturbs the integrity of the FH2 motif since these residues are involved in a number of interactions. Thus, extensive hydrogen-bonding networks are formed between Glu1134 and His1004, Gln1136 and Glu1011, Arg1138 and Glu1008, and Arg1139 and Glu1011 (Figure 3B). Moreover, Val1132 is involved in a hydrophobic core together with Ala1007, Leu1018, and Phe1128 (Figure 3B).

Both Ends of FH2 Are Required for Activity

In order to find out whether both ends of the elongated FH2 protein are required for the inhibition of actin polymerization, we used the structure to design mutants of exposed residues in the most highly conserved regions of the protein surface, as indicated in Figure 4D. When 30 different formin sequences were aligned and the conserved residues were mapped on the surface of the molecule, clustering of conserved residues around Met970 and Ile845 were prominent (only six sequences are shown, Figure 1B). Since hydrophobic residues are rarely exposed to the solvent, we suspected that one or both of these residues are involved in interaction with actin. Therefore, we replaced these hydrophobic residues with the more hydrophilic arginine.

The mutants M970R and I845R were soluble, stable, and could be purified as for the wild-type protein. To investigate the effect of the mutations, the spontaneous

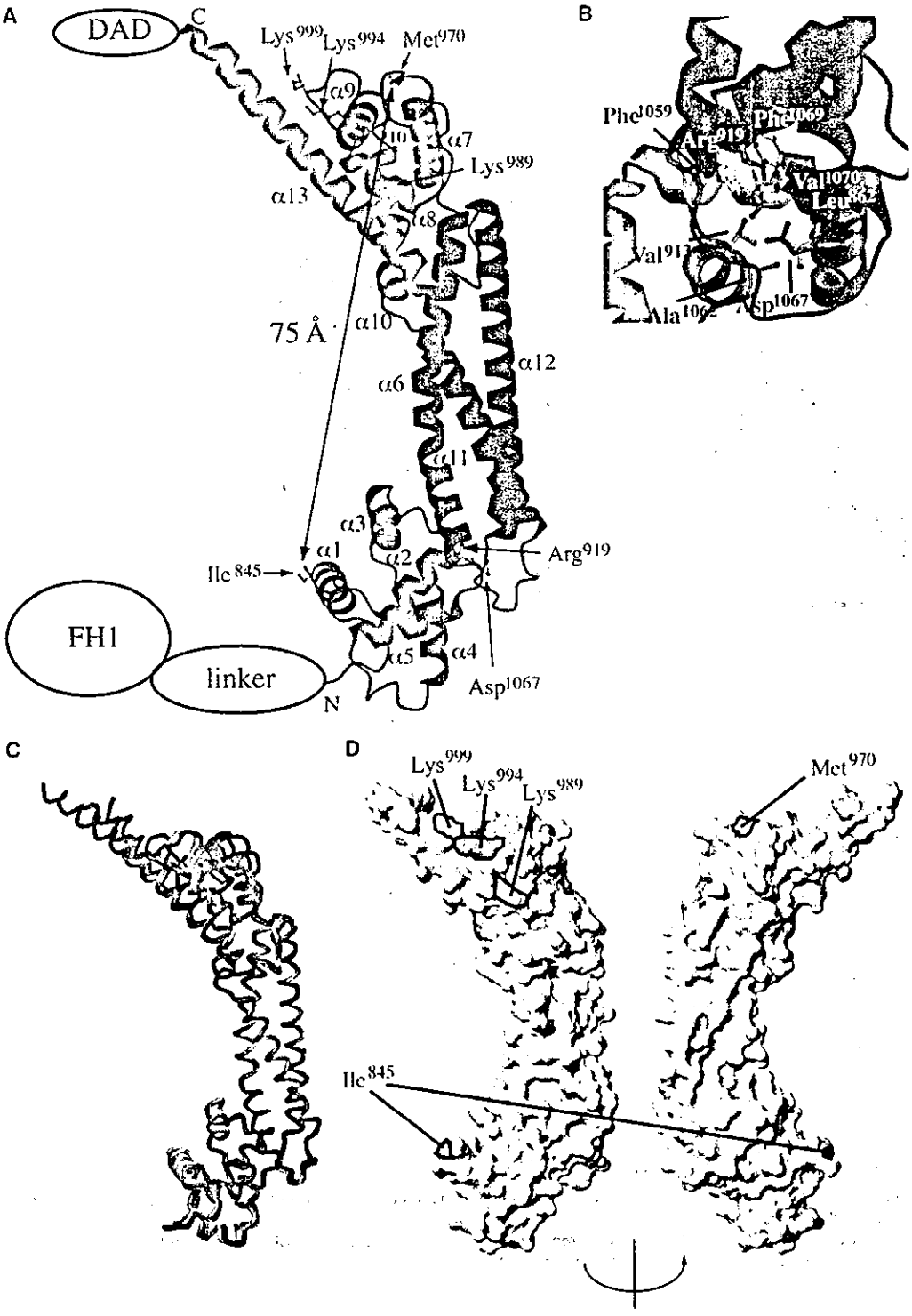

Figure 4. Structural Analysis of the mDia1 Core FH2 Domain

(A) Ribbon diagram of the core FH2 domain. The NH_2-terminal, three-helix-bundle, and FH2 motif subdomains are colored red, blue, and green, respectively. The region corresponding to the highly conserved ^{967}GNXMN^{971} motif is colored purple. The NH_2 and COOH termini of the molecule are indicated by N and C, respectively. Secondary structures are numbered consecutively. Ile845, Met970, Lys989, Lys994, Lys999, Arg919, and Asp1067 are shown as ball-and-stick representation. Distance between Ile845 and Met970 and approximate locations of the FH1 domain, linker, and DAD in mDia1 are indicated.

(B) A buried salt bridge. A salt bridge between Arg919 and Asp1067 is shown as ball-and-stick representation together with surrounding hydrophobic residues, as indicated.

(C) Superimposition of the four molecules in the asymmetric unit. Molecules A, B, C, and D, colored in red, green, blue, and yellow, respectively, were superimposed on the three-helix-bundle subdomains, and are oriented as in (A). Note that the FH2 subdomain exhibited the highest conformational differences.

(D) Conserved residues. Surface representation of the mDia1-FH2 core domain with residues conserved in the six formin family proteins colored orange and those conserved in five of six colored yellow. Residues mentioned in the text are indicated. Left and right: orientation as in Figure 3B and rotated 180°, respectively.

polymerization of actin was measured in the presence of I845R or M970R as for WT (Figure 2E). The effect of the mutants on the actin polymerization was smaller than that of the wild-type mDia1-FH2. Hyperbola fit to the [M970R] dependence of the elongation rates (insert in Figure 2E) gave half saturation at 8.91 ± 3.05 μM, suggesting an approximately four times weaker effect than for the wild-type (1.96 ± 0.43 μM). The fit also indicated that in the presence of saturating [M970R] the elongation rate decreased to 36 ± 6% of that measured in the absence of formin. The effect of I845R was even weaker than that of the M970R. Although the I845R effect did not give a well-defined hyperbola, the results are consistent with a decrease in elongation rate to ~40% with half saturation at ~16 μM, approximately eight times weaker than that of the wild-type mDia1-FH2. Accordingly, at saturating concentrations the mutants can produce the inhibition of the actin polymerization similar to that observed for the wild-type mDia1-FH2, but the half saturation concentrations were approximately four and eight times higher for the M970R and I845R mutants than for the wild-type FH2. The effect of the mutations showed that the proper interaction between mDia1-FH2 and actin requires both ends of the elongated mDia1-FH2 protein.

Discussion

In our experiments mDia1-FH2 and mDia3-FH2 did not appear to induce actin nucleation but rather inhibited the spontaneous polymerization of actin (Figure 2A). The inhibition of actin polymerization in vitro by mDia1-FH2 and mDia3-FH2 is consistent with an in vivo study, which showed that a similar FH2 construct inhibited actin polymerization induced by an activated mDia protein (Copeland and Treisman, 2002). Our data suggest that the core FH2 domain of mDia1 and mDia3 has a subset of properties of longer constructs characterized in previous studies (Pruyne et al., 2002; Pring et al., 2003; Kovar et al., 2003; Li and Higgs, 2003; Zigmond et al., 2003). The effect of mDia1-FH2 and mDia3-FH2 on the depolymerization rate of actin filaments (Figure 2B) and on the critical concentration of actin (Figure 2C) is consistent with the observation that barbed-end capping proteins decrease the dissociation rate of actin monomers from filaments and increase critical concentration of actin assembly (Wear et al., 2003). Although on the basis of our data it is not possible to exclude other mechanisms (such as for example a copolymerization mechanism similar to that observed for microtubule assembly in the presence of colchicine [Stemlicht and Ringel, 1979]), the similarities between our data and the analyses of other formin fragments (Pruyne et al., 2002; Pring et al., 2003; Li and Higgs, 2003; Kovar et al., 2003; Zigmond et al., 2003) suggests that both mDia1-FH2 and mDia3-FH2 are likely to act at the barbed end of actin filaments. Although more work is required to determine the affinity of mDia1-FH2 and mDia3-FH2 for barbed ends, the available data also suggest that the affinity may be about three orders of magnitude weaker than that of longer constructs.

The comparison of the detailed analysis of budding yeast Bni1p (Pruyne et al., 2002; Pring et al., 2003; Zigmond et al., 2003), fission yeast Cdc12p (Kovar et al., 2003), and mDia1 (Li and Higgs, 2003) fragments with our data indicates that mDia1-FH2 resembles properties of Bni1, which caused partial barbed-end capping (Pruyne et al., 2002; Pring et al., 2003; Zigmond et al., 2003). Both FH2 and FH1FH2 Bni1p fragments inhibited barbed-end elongation to ~50% and the depolymerization rate to ~60%, while the critical concentration showed no change in the presence of the fragments (Zigmond et al., 2003), in agreement with the conclusion that mDia1 was more similar to Bni1p than to Cdc12p (Li and Higgs, 2003). It appears that both mDia1 and Bni1p act through a leaky barbed-end capping mechanism. The mDia3-FH2 fragment, however, is more similar to the construct containing the FH2 domain of the fission yeast formin, Cdc12p, which tightly caps barbed ends and acts as a classic barbed-end capping protein (Kovar et al., 2003). Cdc12p(882–1375) was shown to decrease the actin depolymerization rate to 34%, to inhibit barbed-end elongation, and to increase the critical concentration to 0.9 μM. To determine the physiological significance of the differences between the observations with Cdc12p, Bni1p, and mDia, more experimental work and direct experimental comparisons are required.

While longer mDia1 fragments were previously reported to accelerate actin polymerization (Li and Higgs, 2003), our experiments showed that mDia1-FH2 and mDia3-FH2 inhibited spontaneous actin assembly. We thus set out to define a minimal length FH2-containing fragment which is able to accelerate polymerization. An mDia3 fragment containing the core FH2 domain and a linker region which connects FH2 and FH1 (mDia3-FH2+linker, see Figure 1A), whose N-terminal domain boundaries were close to those identified as being functional for actin polymerization in vivo (Copeland and Treisman, 2002), accelerated actin polymerization at subnanomolar concentrations under conditions previously applied for the FH2 fragments (Figure 5A). Above 2.5 nM mDia3-FH2+linker the initial parts of the pyrene transients were within the mixing time. Below this concentration the mDia3-FH2+linker dependence of the elongation rate was linear (insert in Figure 5A).

We find a tetramer of FH2 in the asymmetric unit (Figure 3A), where only the A/B and C/D molecules have a large, albeit not very complementary, surface area of interaction (2350 Å^2). The tetramer in the crystal could be an artifact of crystal packing. Size exclusion analysis of the mDia1-FH2 indeed gives an apparent molecular mass of 67 kDa (Figure 5B), which is between that expected for a dimer and a monomer. Considering the elongated nature of the FH2, it is unlikely that a dimer of the elongated FH2 would elute later than a value calculated for a spherical particle. The longer mDia3-FH2+linker eluted much earlier than mDia1-FH2 and gave an apparent molecular mass of more than 200 kDa. Although gel filtration analysis in principle only gives the Stokes' radius of proteins, the apparent dimerization or oligomerization of the mDia3-FH2+linker construct (Figure 5B) is completely in line with previous studies on mDia1(748–1255) (Li and Higgs, 2003), Bni1p(1227–1324), and Bni1p(1348–1824), which led the authors to suggest that the ability of formins to oligomerize allows them to walk processively with the barbed end as the filament elongates (Zigmond et al., 2003). The finding

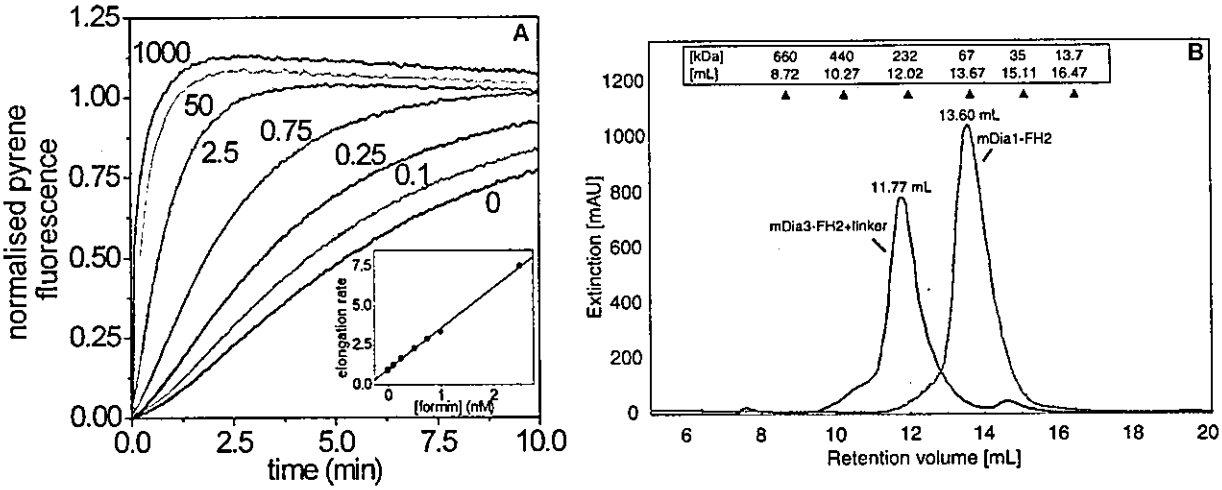

Figure 5. The Linker Dramatically Alters the Properties of the Core FH2 Domain

(A) Actin polymerization. Actin was polymerized by simultaneously adding 10 mM KCl, 0.5 mM MgCl2, and mDia3-FH2+linker to actin monomer solutions (3.5 μM, 5% pyrene-labeled). The figure shows the normalized pyrene fluorescence transients in the absence of formin (black) and in the presence of increasing mDia3-FH2+linker concentrations in nM as indicated. The insert shows the [mDia3-FH2+linker] dependence of the relative elongation rate determined from the slopes at 50% saturation of the reaction (linear fit is shown as solid line).

(B) Gel permeation chromatography of mDia1-FH2 and mDia3-FH2+linker. The elution profiles of mDia1-FH2 and mDia3-FH2+linker are colored gray and black, respectively. Elution volume and corresponding calculated molecular weight are indicated above the profiles. Elution volumes (in ml) and molecular masses (kDa) of marker proteins are shown above.

that fragments covering the FH2 domain of FHOD1/Fhos bind to each other (Takeya and Sumimoto, 2003) further supports the importance of oligomerization for the function of formins.

Previous studies have shown that a dimeric protein binding to two adjacent actin monomers in a filament can bind with an affinity more than 100-fold tighter than the equivalent monomer provided that the relative geometry of the two pairs of binding sites is appropriate. The classic case is the dimeric fragment of myosin II, heavy meromyosin, which binds two actin monomers with an affinity more than 100-fold tighter than the equivalent monomeric fragment subfragment 1 (K_D of 2×10^{-10} and 2×10^{-7} M, respectively; see Goody and Holmes, 1983, and Conibear and Geeves, 1998, for a full discussion). The reduced affinity of the core FH2 domain compared to the longer FH2 plus linker can thus be accounted for by the dimerization (or higher oligomerization) of the longer fragment. This implies that the linker region is essential for nucleation and for dimerization and that the tight affinity for actin and nucleation of actin polymerization are both properties of the dimer. Crystallization of the longer fragment will be needed to address this issue.

We thus conclude that, while the core FH2 domain binds to actin and inhibits actin polymerization, it is the 72 residue linker between the FH2 and FH1 domain which dramatically changes the property of the fragment. It provides the structural framework for oligomerization, for increasing the affinity with F-actin, and for inducing actin polymerization. Further structural and biochemical studies will be necessary to clarify the exact mechanism mediated by the linker fragment.

Experimental Procedures

Protein Preparations

Complementary DNA for full-length mDia3 was isolated by polymerase chain reaction-based cloning, and its nucleotide sequence has been deposited in GenBank (AY 312280) (S. Yasuda and S.N, unpublished data). The FH2 domains of mouse mDia1 and mDia3 were expressed as GST-fusion proteins in the *E. coli* strain BL21 (DE3) pLysS. GST-fusion proteins were loaded onto a GSH column (Pharmacia), eluted from the column after cleavage by thrombin and further purified by size exclusion chromatography (for details see Supplemental Data at http://www.molecule.org/cgi/content/full/13/4/511/DC1). The mDia3-FH2+linker was prepared in the same way as the other FH2 constructs described above. Rabbit skeletal actin was prepared as described previously (Spudich and Watt, 1971) and gel filtered through a Sephadex G100 column. Pyrene labeling was carried out according to Criddle et al. (1985).

We measured concentrations of mDia samples with Bradford method (using BSA as standard) and confirmed the values with a method based on extinction coefficients of proteins in guanidine hydrochloride. The deviation between values obtained from both the methods were less than 30%. We used the concentrations from the Bradford method for interpretation.

Fluorescence Experiments

Freshly prepared unlabeled and pyrene-labeled Ca-G-actin in 4 mM Tris/HCl (pH 7.4), 0.2 mM ATP, 0.1 mM $CaCl_2$, 0.5 mM DTT were clarified by ultracentrifugation (100,000 g, 2 hr, 4°C) before the experiments. In spontaneous actin assembly measurements mDia1-FH2 or mDia3-FH2 fragments were added to actin monomer solutions (5% pyrene-labeled) and the samples were incubated for 5 min with 200 μM EGTA and 50 μM $MgCl_2$ at 22°C to exchange the actin bound Ca^{2+} for Mg^{2+}. The polymerization was started by addition of KCl and $MgCl_2$ to 10 mM and 0.55 mM, respectively. The longer mDia3 fragment (mDia3-FH2+linker) induced actin polymerization during the cation exchange. Therefore, these fragments were added to the actin solution after the cation exchange was completed together with the KCl and $MgCl_2$. In actin depolymerization experiments, 5 μM actin (68% pyrene-labeled) was polymerized (10 mM KCl, 0.5 mM $MgCl_2$) for at least 4 hr and then diluted into polymerization buffer alone, or into polymerization buffer supplemented with mDia1-FH2 or mDia3-FH2. In critical concentration experiments, actin (between 0 and 20 μM) was incubated with fixed concentrations of mDia1-FH2 or mDia3-FH2 in polymerization buffer overnight, and then the fluorescence intensity of the samples was measured. In all experiments, the pyrene fluorescence changes were monitored with excitation and emission wavelengths of 365 and 407 nm, respectively. The fluorescence experiments were carried out with a

Cary Eclipse Fluorescence Spectrophotometer (Varian) or a Perkin-Elmer LS50B Spectrofluorimeter at 22°C.

Cosedimentation Assay

Actin filaments (3 μM) were mixed with mDia1-FH2 or mDia3-FH2 at different concentrations and incubated for 30 min at room temperature. The samples (100 μl) were centrifuged at 600,000 g for 30 min at 4°C, and the pellets and supernatants were separated. One hundred microliter SDS-PAGE sample buffer was added to the supernatants. The pellets were dissolved in 100 μl distilled water, and 100 μl SDS-PAGE sample buffer was added to each tube. These samples were then applied to 12.5% SDS-PAGE gels. The affinity of FH2 for actin (K_D) was estimated from the results of polyacrylamide gel analysis (Figure 2) using the following equation (Kurzawa and Geeves, 1996):

$$[A]_0 S^2 - ([A]_0 + [FH2]_0 + K) S + [FH2]_0 = 0 \quad (1)$$

where $[A]_0$ and $[FH2]_0$ are the total actin and FH2 concentrations, respectively, and S is the fraction of FH2 bound to actin (calculated as the ratio of density of FH2 bands to those of actin bands in the pellets).

Crystallization, Data Collection, and Structure Determination

The mDia1-FH2 was purified as described above and concentrated to approximately 20 mg/ml prior to crystallization. Crystals were grown at 20°C using the hanging-drop vapor-diffusion method by mixing the protein in 1:1 volume ratio with a solution containing 20% (*v/v*) PEG3350 (Sigma) and 200 mM Na_2SO_4. Crystals were harvested in a solution containing 10% (*v/v*) PEG3350, 100 mM Na_2SO_4, and 18% (*v/v*) glycerol and flash-frozen in liquid nitrogen. A native data set to 2.6 Å resolution was collected at 100 K at ID14-1 beamline at the European Synchrotron Radiation Facility (ESRF) in Grenoble, France (Table 1). The selenomethionine (SeMet) substituted protein was expressed in the *E. coli* strain BL21 (DE3) pLysS growing in minimal medium in which methionine was replaced by SeMet. The SeMet-substituted protein crystals were grown at 20°C using the hanging-drop vapor-diffusion method by mixing the protein in 1:1 volume ratio with a solution containing 20% (*v/v*) PEG3350 and 200 mM KSCN. The SeMet crystals were harvested in a solution containing 10% (*v/v*) PEG3350, 100 mM KSCN, and 21% (*v/v*) glycerol and flash-frozen in liquid nitrogen.

A SAD data set with a resolution of 3.4 Å resolution was collected at the selenium edge at the ID29 beamline at the ESRF (Table 1) and processed with the HKL suite (Otwinowski and Minor, 1997) and/or XDS (Kabsch, 1993). SnB (Weeks and Miller, 1999), SHELXD (Usón and Sheldrick, 1999), and SOLVE (Terwilliger and Berendzen, 1996) were used to identify 32 selenium sites that were refined with SHARP (de La Fortelle and Bricogne, 1997). The initial phases were calculated by SHARP using 52 selenium sites (32 plus 20 additional ones located by SHARP) and were improved by DM (CCP4, 1994), resulting in a readily interpretable map to which most of the backbone of all four molecules in the asymmetric unit could be positioned using O (Jones et al., 1991). The preliminary model of a monomer with side chains was used for molecular replacement into the native crystal (Table 1) using the program AmoRe (CCP4). The best solution had a correlation coefficient of 43.8 and R factor of 47.9% (second best: correlation coefficient 38.6, R factor 49.8%). Manual rebuilding was performed for ambiguous parts using simulated annealing omit electron density maps. Iterative rounds of rebuilding and refinement were performed, and more residues were added. Initial NCS constraints were relaxed gradually during refinement after the significant differences between the relative domain positions of the molecule pairs A/C and B/D became apparent. Three sulfate ions were also modeled into strong electron densities close to molecules A, B, and C. Refinement was done by the program CNS (Brunger et al., 1998) and REFMAC (CCP4). Figures were generated using MolScript (Kraulis, 1991), Raster3D (Merrit and Murphy, 1994), and MOLMOL (Koradi et al., 1996).

Analytical Gel Filtration

Analytical gel filtration was performed on Superdex 200 in 50 mM Tris-HCl buffer (pH 7.3) containing 50 mM NaCl, 5 mM DTE, and 5% glycerol.

Acknowledgments

We thank Shingo Yasuda for providing us with mouse mDia1 and mDia3 clones. We thank Katja Kossmeier for the gel filtration experiments. We thank Ilme Schlichting, Wulf Blankenfeldt, Roman Fedorov, and Axel Scheidig for collecting data sets at the ESRF and the Swiss Light Source (SLS), Paul Scherrer Institute, Villingen, Switzerland. We are grateful for the outstanding support at beamlines ID14-1 and ID29 (ESRF) and X06SA (SLS). This work was supported by Deutsche Forschungsgemeinschaft grant JAP-113/219/01 (to A.W. and S.N.), by a grant-in-aid for Scientific Research from the Ministry of Education, Science and Culture of Japan (to A.W. and S.N.), by European Union grant HPRN-CT-2000-00091 (to M.A.G.), and by a Hungarian Scientific Research Fund (OTKA) grant T043103 (to M.N.). A.S. was supported by the Alexander von Humboldt Foundation. M.N. is an EMBO/HHMI Scientist.

Received: September 2, 2003
Revised: January 12, 2004
Accepted: January 13, 2004
Published: February 26, 2004

References

Alberts, A.S. (2001). Identification of a carboxyl-terminal diaphanous-related formin homology protein autoregulatory domain. J. Biol. Chem. *276*, 2824–2830.

Brunger, A.T., Adams, P.D., Clore, G.M., DeLano, W.L., Gros, P., Grosse-Kunstleve, R.W., Jiang, J.S., Kuszewski, J., Nilges, M., Pannu, N.S., et al. (1998). Crystallography & NMR system: a new software suite for macromolecular structure determination. Acta Crystallogr. D Biol. Crystallogr. *54*, 905–921.

Castrillon, D.H., and Wasserman, S.A. (1994). Diaphanous is required for cytokinesis in Drosophila and shares domains of similarity with the products of the limb deformity gene. Development *120*, 3367–3377.

Chai, J., Du, C., Wu, J.W., Kyin, S., Wang, X., and Shi, Y. (2000). Structural and biochemical basis of apoptotic activation by Smac/DIABLO. Nature *406*, 855–862.

CCP4 (Collaborative Computational Project, Number 4) (1994). Acta Crystallogr. D Biol. Crystallogr. *50*, 760–763.

Conibear, P.B., and Geeves, M.A. (1998). Cooperativity between the two heads of rabbit skeletal muscle heavy meromyosin in binding to actin. Biophys. J. *75*, 926–937.

Copeland, J.W., and Treisman, R. (2002). The Diaphanous-related formin mDia1 controls serum response factor activity through its effects on actin polymerization. Mol. Biol. Cell *13*, 4088–4099.

Criddle, A.H., Geeves, M.A., and Jeffries, T. (1985). The use of actin labelled with N-(1-pyrenyl)iodoacetamide to study the interaction of actin with myosin subfragments and troponin/tropomyosin. Biochem. J. *232*, 343–349.

de La Fortelle, E., and Bricogne, G. (1997). Maximum-likelihood heavy-atom parameter refinement for multiple isomorphous replacement and multiwavelength anomalous diffraction methods. Acta Crystallogr. A *276*, 472–494.

Djinovic-Carugo, K., Young, P., Gautel, M., and Saraste, M. (1999). Structure of the α-actinin rod: molecular basis for cross-linking of actin filaments. Cell *98*, 537–546.

Evangelista, M., Blundell, K., Longtine, M.S., Chow, C.J., Adames, N., Pringle, J.R., Peter, M., and Boone, C. (1997). Bni1p, a yeast formin linking cdc42p and the actin cytoskeleton during polarized morphogenesis. Science *276*, 118–122.

Evangelista, M., Pruyne, D., Amberg, D.C., Boone, C., and Bretscher, A. (2002). Formins direct Arp2/3-independent actin filament assembly to polarize cell growth in yeast. Nat. Cell Biol. *4*, 260–269.

Fernandez, I., Ubach, J., Dulubova, I., Zhang, X., Sudhof, T.C., and Rizo, J. (1998). Three-dimensional structure of an evolutionarily conserved N-terminal domain of syntaxin 1A. Cell *94*, 841–849.

Goody, R.S., and Holmes, K.C. (1983). Cross-bridges and the mechanism of muscle contraction. Biochim. Biophys. Acta *726*, 13–39.

Grum, V.L., Li, D., MacDonald, R.I., and Mondragón, A. (1999). Struc-